Uncovering the Origins of Selectivity in Non-Heme Iron Dioxygenase-Catalyzed Tropolone Biosynthesis

Taveechai Wititsuwannakul,[1] Kevin C. Skinner,[1,2] Joshua A. Kammeraad,[1] Di Yang,[1,2] Alison R. H. Narayan,[1,2] Paul M. Zimmerman[1]*

[1]Department of Chemistry, University of Michigan, Ann Arbor, Michigan 48109, USA

[2]Life Sciences Institute, University of Michigan, Ann Arbor, Michigan 48109, USA

E-mail: paulzim@umich.edu

Abstract

Non-heme iron (NHI) enzymes perform diverse oxidative transformations with precise control that is not easily available to small molecule catalysis, such as the biosynthesis of tropolone. Among them, Anc3, a reconstructed ancestral α-ketoglutarate (α-KG) dependent NHI dioxygenase, catalyzes a ring-expansion in the tropolone biosynthesis from cyclohexadienone to afford tropolone natural product stipitaldehyde (ring-expansion product) alongside 3-hydroxyorcinaldehyde (shunt product). This study reveals how the enzyme environment guides the reaction to ring-expansion product preferably over shunt product, where the precise selectivity ratio depends on just a handful of residues. In particular, molecular dynamics (MD) and quantum mechanical/molecular mechanical (QM/MM) simulations describe how the substrate binds within the NHI active site and can proceed through two distinct mechanisms, ring-expansion or rebound hydroxylation, to yield the two experimentally observed products. Discovery of a linear relationship of ΔE_a values and hydrogen bond distances between Arg191 and the Fe(III)–OH group reveals that inhibition of the rebound hydroxylation step increases selectivity towards ring-expansion. Our findings suggest that the rebound hydroxylation rate is further tuned through the Fe(III)–OH bond strength, as influenced by specific secondary sphere coordination effects around the active site. These influences are largely orthogonal to the ring-expansion mechanism, which is shown to prefer to proceed through a radical pathway. In addition, a cationic pathway initiated by electron transfer from substrate to iron is ruled out based upon thermodynamic infeasibility. Altogether, the atomistic details and reaction mechanisms delineated in this work have the potential to guide the tuning of reaction pathway in related NHI enzymes for selective oxidation reactions.

Key words: non-heme iron dioxygenase, Anc3, MD, QM/MM, ring-expansion, rebound hydroxylation, hydrogen bond

■ Introduction

Iron-containing enzymes are essential for the regulation of numerous biological processes, i.e., DNA and RNA base repair,[1] oxygen homeostasis,[2] biosynthesis of hormones,[3] and metabolism of drugs.[4] In addition, these enzymes play essential roles in a variety of natural product biosynthetic reactions.[5] Among them, α-ketoglutarate (α-KG) dependent non-heme iron (NHI) dioxygenases are functionally-diverse enzymes which perform a wide range of chemical transformations with exquisite control over chemo-, site- and stereoselectivity to afford structurally-complex natural products.[5a-c,6] As such, α-KG-dependent NHI dioxygenases have attracted attention for their application as catalysts for challenging reactions, for instance the ring-expansion reactions shown in Figure 1a.[7,8]

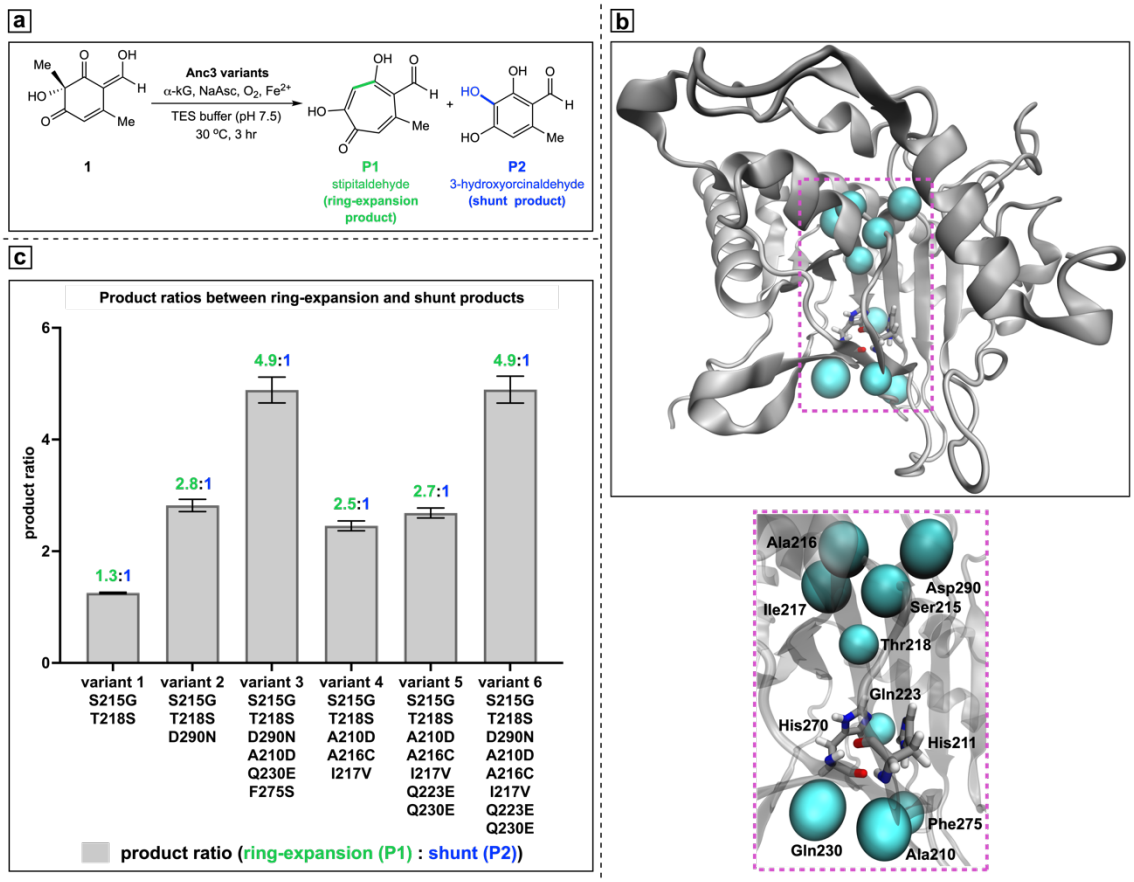

Figure 1. (a) Anc3 variants-catalyzed oxidative transformation of **1** to **P1** and **P2**. (b) 3D enzyme model of the wild-type Anc3 constructed by AlphaFold2 with key amino acid residues (blue ovals) for mutational analysis. (c) Product ratios between **P1** and **P2**, depending upon Anc3 variants.

Tropolones are a structurally-diverse group of bioactive metabolites containing aromatic cycloheptatrienes with an α-hydroxyketone moiety (such as **P1** in Figure 1a).[9] While examples of

organic synthesis of tropolones through rearrangements such as ring-expansion are available,[9,10] they require extensive prefunctionalization and laborious efforts to achieve desired substitution patterns of the tropolone natural products, resulting in limited access of target compounds.[10] As an alternative to conventional synthetic approaches, α-KG-dependent NHI dioxygenases have evolved to catalyze skeletal rearrangements with high site- and stereoselectivity to afford a variety of natural products.[5a-c,6-8,11] Among them, TropC, an α-KG-dependent NHI dioxygenase from biosynthesis of tropolone natural product stipitatic acid in *Talaromyces stipitatus*, is an efficient biocatalyst for the oxidative ring-expansion of cyclohexadienone **1** to the tropolone product, stipitaldehyde (**P1**, ring-expansion product), with little 3-hydroxyorcinaldehyde (**P2**, a shunt product in stipitatic acid biosynthesis) also being formed (Figure 1a).[7] Recently, Anc3, a reconstructed ancestral α-KG dependent NHI dioxygenase which shares 59% sequence identity with TropC, was also shown to transform **1** to **P1** as well as **P2** (Figure 1a).[7c,8] Product ratios between **P1** and **P2** were found to sensitively depend upon Anc3 variants. Surprisingly, changes in just a few amino acid residues resulted in substantial shifts in the reaction selectivity (Figure 1b,c), especially the increases in the product ratios from 1.3:1 of variant 1 to 2.8:1 of variant 2 with just one mutation at the active site. With four and six mutations, ratios of 4.9:1 (variants 3 and 6) were achieved.[8] These findings motivated detailed investigations into the underlying reaction mechanisms and sources of reactivity control.

Enzymes from the same protein family may perform different functions while still sharing common mechanistic features.[12] NHI-catalyzed reactions are believed to involve Fe(IV)–oxo centers[6,13,14] such as [Fe(IV)=O] which activate a C–H bond and form a radical intermediate such as **4** + [Fe(III)–OH] (Figure 2).[5a-c,6-8,11] After the radical intermediates are generated, reaction pathways may bifurcate, and the structural features which control reaction selectivity are generally not well understood. For skeletal rearrangements, radical as well as polar mechanisms (including single electron transfer; SET) have been proposed for NHI enzymes.[5a-c,6-8,11,15] In addition, the activated substrate can proceed through various radical-based reaction steps, i.e., hydroxylation, ring-expansion, ring-contraction, desaturation, halogenation, endoperoxidation, and epimerization,

each resulting in a different reaction outcome.[5a-c,6-8,11,15] These diverse reaction pathways are a crucial feature of NHI enzymes and might be exploited to reach specified products. Accordingly, gaining insights into NHI mechanistic details, structural features,[16] and how the fate of the radical species is controlled can rationalize the origins of the selectivity and pave the way for the development of novel synthetic transformations.

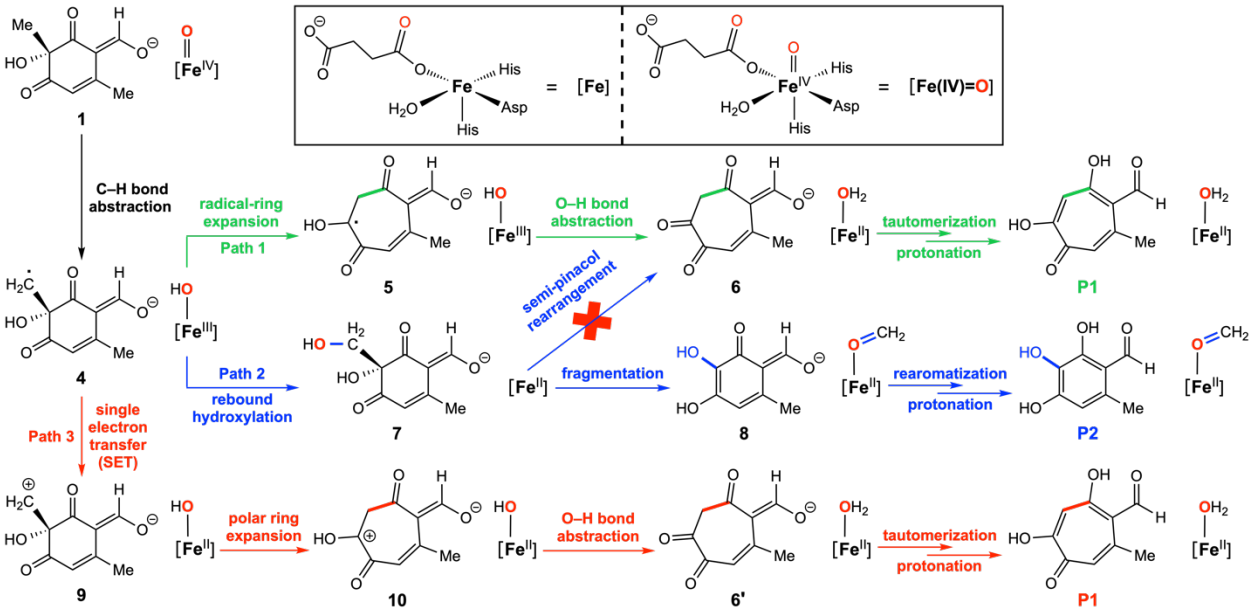

Figure 2. Proposed mechanisms of Anc3-catalyzed oxidative transformations associated with C–H bond abstraction of **1** + [Fe(IV)=O] to afford the key radical species **4** + [Fe(III)–OH], followed by three possible pathways (Path 1 (radical ring-expansion, green), Path 2 (rebound hydroxylation, blue), and Path 3 (SET, red)), leading to **P1** and **P2**.

As Anc3 and TropC are in the same protein family,[7c,8] their mechanistic details for the oxidative transformations of **1** to **P1** and **P2** could be similar (Figure 2). Based upon the experimental observations of Anc3 indicating that **P1** is the dominant product (Figure 1),[8] Path 1 (radical ring-expansion) or 3 (SET) is more favorable than rebound hydroxylation (Path 2) under the reaction conditions. Our groups have used computations in conjunction with experimental investigations to provide viable hypotheses for the mechanisms of these transformations.[8] This study was consistent with formation of **P1** in TropC through radical ring-expansion (Path 1; Figure 2).[7c] This path is also supported by literature showing that tropolones could be synthesized from cyclohexa-2,4-dienones through radical-based rearrangement.[10b,c] Another possible pathway to **P1** involves SET (Path 3), which also has been proposed as operating within several other NHI enzymes.[15,17]

To afford **P2** in TropC, we suggested that the radical intermediate could proceed through rebound hydroxylation (Path 2) and subsequent fragmentation,[7c] as opposed to the commonly proposed mechanism in literature, polar ring-expansion pathway through rebound hydroxylation and subsequent semi-pinacol rearrangement to generate **P1**.[7a,b] This pathway was evidenced by the observation that hydroxylation product **7**, generated *in situ*, entered the TropC active site and underwent fragmentation to generate **P2**.[7c] Computations also indicated that fragmentation is substantially more energetically accessible than semi-pinacol rearrangement (see the Result section for more details).[7c] Overall, Paths 1-3 are potential reaction pathways starting from **4** + [Fe(III)–OH] for oxidative transformations of **1** catalyzed by Anc3 variants.

The selectivity observed in experiment, in which ring-expansion (Path 1 or 3) is more dominant than rebound hydroxylation (Path 2), has yet to be clearly explained by mechanistic models. The previous study of the divergent reactivities of Anc3 variants 1, 2, 3, and 6 revealed a key hydrogen bond between the substrate and the hydroxyl ligand on the iron center.[8] This hydrogen bond can slow the transfer of the hydroxyl ligand to the substrate. However, beyond this factor, there are numerous influences of the first- and second-coordination spheres around the reaction site which alter substrate binding and positioning, viability of individual reaction mechanisms, and ultimately reaction selectivity.[16] Thus, for Anc3, how enzyme environments mediate the observed selectivity is not yet understood and remained as a big knowledge gap. In particular, it is not known why substitution of just a small number of residues results in significant changes in the selectivity as mentioned above (Figure 1c).

Molecular dynamics (MD) and quantum mechanical/molecular mechanical (QM/MM)[18] simulations are highly useful tools for exploring reaction mechanisms of enzymes.[19] These tools are especially useful for identifying transient structures and reaction pathways that cannot easily be isolated in experiment. This information can explain how reaction selectivity is achieved and how alternative product channels are blocked in enzyme active sites.[16] These methods have also been used for validating correlations between enzyme mutations and their selectivity and exploring how their changes in enzyme environments due to mutations modulate the activation barriers.[20]

Based upon these precedents, our use of MD and QM/MM simulations is likely to provide significant insights into mechanisms for Anc3 catalysis and information on what steers Anc3 variants to produce **P1** over **P2**.

To address the key question of how enzyme environments dictate the reaction selectivity in Figure 1c, combined MD and QM/MM simulations which delineated the atomistic reaction pathways were performed to explore the most feasible mechanisms of Anc3 variants-catalyzed oxidative transformation of **1**. These mechanistic details are essential for probing the sources of the selectivity leading to bifurcation products (dominant ring-expansion product **P1** vs. little shunt product **P2**), which can establish relationships between substitutions of key amino acid residues in the active sites and the substantial changes in selectivity with enzyme variants. Key non-covalent interactions in the active sites distinguish radical ring-expansion, rebound hydroxylation, and SET reactivities. In all, this study provides a foundation for understanding α-KG dependent NHI dioxygenase reaction selectivity[7c,8] and giving inspiration for rational design of NHI enzymes.

■ Computational Details

The Visual Molecular Dynamics (VMD) software program[21] was employed for all 3D images and spin density plots (isovalue 0.2 au). IQmol[22] was used to visualize molecular orbitals (isovalue 0.2 au).

1. Model Preparation. As Anc3 originated from the ancestral sequence reconstruction process and no crystal structure is available,[8] a model was built using the AlphaFold2 software[23] from its amino acid sequence. To gain insights into how key amino acid residues of Anc3 influence mechanistic details, structural features, and reaction selectivity on the enzymatic reaction in Figure 1a, mutations were made to specific residues. The residues of interest were shown in Figure 1b, corresponding to Anc3 variants:

Variant 1: S215G T218S

Variant 2: S215G T218S D290N

Variant 3: S215G T218S D290N A210D Q230E F275S

Variant 6: S215G T218S D290N A210D A216C I217V Q223E Q230E

The approaches in this work followed the procedures from the previous studies of the NHI enzymes in the same protein family.[7c,8] The X-ray crystal structure of the α-KG NHI enzyme, thymine-7-hydroxylase (T7H) of *Neurospora crassa* possessed structural similarity to Anc3 (Protein Data Bank (PDB)[24] ID, 5C3Q; sequence identity, 29%),[25] which contains the nickel atom, α-KG cofactor, and thymine (native substrate) in the active site, was used as a template for the Anc3 active sites (Figure 3). To build the Anc3-substrate-α-KG complexes, the nickel, thymine, and α-KG coordinates of T7H were transferred to the Anc3 variant models. The nickel atom was changed to iron, and thymine was replaced with **1** by docking with the AutoDock Vina software package,[26] based upon the substrate-bound enzyme models which were experimentally validated by alanine screening of the enzyme in the same protein family, TropC (6XJJ).[7c] In addition, the first-coordination sphere of the iron of Anc3 variants was modelled to match that of TropC since their active sites are similar (see Section S1.1.1 of the Supporting Information (SI)) and the residues which hydrogen bond to succinate and Asp213 are identical and well overlaid (Figure S1 (SI)). The water ligand was then included in the first-coordination sphere of iron for Anc3 variants like TropC.[7c] Further details are available in Section S1.1.1 (SI).

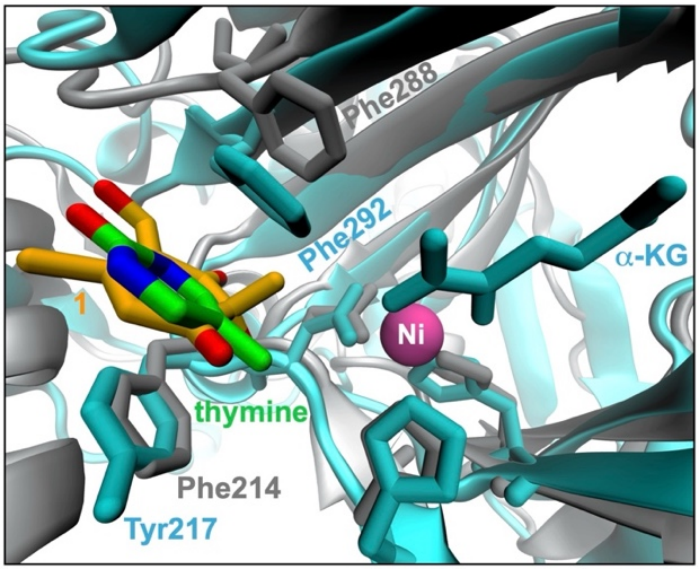

Figure 3. Overlaid structures at the active sites of T7H (chain A) and wild-type Anc3. T7H is pictured in cyan with thymine shown in green, α-KG in cyan, Tyr217 and Phe292 in cyan, and nickel in pink, and Anc3 is pictured in gray with **1** shown in orange and Phe214 and Phe288 in gray.

Missing hydrogen atoms and protons were added to the Anc3 variant models according to their canonical protonation states using the CHARMM-GUI.[27] The protonation states at pH 7.5 were determined with the Propka-3.1 software,[28] and the tautomeric forms of histidine were assigned to maximize their hydrogen bonding interactions. To ensure electric neutrality of the models, potassium and chlorine counterions were added at random positions, using the CHARMM-GUI. The atom counts of counterions for each model are summarized in Table S2 (SI). A water box was used with periodic boundary conditions to construct solvent environment, and the particle mesh Ewald method[29] was applied to describe long-range electrostatic effects. Dimensions of the water boxes were established to fit the largest dimensions of proteins plus 10 Å. All water molecules within 2.8 Å of heavy atoms were removed. Force field parameters for **1** and α-KG were obtained using CGenFF 4.0,[30] and parameters for the iron atom were taken from the previous study by Pang *et al*.[31] A set of constraints based upon the T7H crystal structure[25] were used to initially refine the Anc3 geometries (see Section S1.1.2 (SI)). The restrained structures were subjected to 5,000 step molecular mechanics (MM) geometry optimizations using the steepest decent algorithm and the CHARMM36 force field.[32] These optimized structures formed the basis of the MD sampling of the next subsection.

2. Classical MD Simulations and Analysis. A series of MD simulations were carried out with the OpenMM/CHARMM[33] interface (version c45a2) using periodic boundary conditions, the particle mesh Ewald for long-range electrostatic interactions, a 2 fs timestep, and a Langevin thermostat[34] (friction coefficient = 5 ps^{-1}). To equilibrate the models, a three step MD protocol was conducted. In the first phase, the restrained active sites mentioned in Section S1.1.2 (SI) and harmonic restraints of 10.0 kcal/(mol$Å^2$) on all heavy atoms of the solute were applied, and the models were slowly heated from 10 K to 298 K over 500 ps. In the second phase, the harmonic restraints were removed, and the temperature was kept constant for an additional 500 ps. In the final phase, the Phe214 positional restraint was removed, while other restraints were maintained. Simulations were performed for 12 ns, in which the first two ns were used for equilibration.

The extent of equilibration of each Anc3 variant model was determined based upon a root-mean square deviation (RMSD) plot of the protein backbone showing small fluctuations (Figures S2-S5 (SI)). To obtain **1** + [Fe(IV)=O] structures in which the C–H bond is ready for abstraction, one MD snapshot from each equilibrated enzyme model was selected based upon structural parameters of C–H bond abstraction between **1** (C_1 and H_4) and the iron-coordinated oxygen (O_1) of α-KG (H_4–O_1 < 2.72 Å (the sum of van der Waals (vdW) radii of H_4 and O_1 atoms)[35] and ∠C_1–H_4–O_1 ~ 110-180°);[36] see Figures S22-S26 and Table S3 (SI)). These parameters are relative to the coordinated α-KG cofactor rather than the oxo ligand of **1** + [Fe(IV)=O] species[14] (Figures 4 and S35-S38). Subsequently, 5,000 step MM geometry optimizations were performed on each selected MD snapshot, so that a local minimum of each model was obtained. The α-KG structures were then modified to succinate and the oxo ligand for reflecting the active species **1** + [Fe(IV)=O]. Full details of Anc3 variant model preparation are summarized in Sections S1.1, S1.3, and S1.4 (SI). These structures with the chemically realistic active sites were subsequently used in QM/MM models.

3. QM/MM Simulations. The modified **1**+ [Fe(IV)=O] models derived from MD simulations were pruned of all water molecules and counterions within 30 Å of the iron atom. All atoms within 20 Å of the iron atom were allowed to relax, while the rest of the systems were kept frozen. The QM regions were defined to include the iron atom, amino acid residues summarized in Table S4 (SI), substrate **1**, succinate, and oxo and water ligands, and the MM regions for the remaining residues, water (solvent), and counterions. Link atoms between QM and MM regions were automatically placed by pDynamo 3.0.9,[37] a Python program which performs QM and QM/MM simulations, to saturate the valences and simulate the valence bonds at the interface between QM and MM regions. Total atom counts in the QM regions and QM/MM models and the net charges of the QM clusters of Anc3 variants are summarized in Table S4 (SI).

All QM/MM simulations were conducted with pDynamo 3.0.9 utilizing the limited-memory Broyden-Fletcher-Goldfarb-Shanno (L-BFGS) optimizer.[38] During QM/MM geometry optimizations, the QM regions were treated by Q-Chem 5.2[39] with the unrestricted B3LYP hybrid func-

tional,[40] which was implemented using the D3 version of Grimme's dispersion function with Becke-Johnson damping (referred to as D3BJ),[41] and the 6-31G(d) basis set,[42] whereas the MM regions were treated with the CHARMM27 force field.[43] The electronic embedding scheme was used to represent the bidirectional electrostatic interactions between the QM and MM regions.[44] While **1**+ [Fe(IV)=O] species (Figures 4 and S35-S38) can sometimes have a triplet spin ground state (2S +1 = 3) outside of enzymes, such as biomimetic complexes, they typically have a quintet spin ground state (2S +1 = 5) within enzyme active sites.[7c,8,14,15b,c,17e,f,45,46] Calculations in different spin states also indicated that the quintet spin state is the ground state of **1** + [Fe(IV)=O] (see Section S2 (SI)). All models were therefore simulated in the quintet spin state.

All QM/MM reaction pathway simulations were performed using the methods mentioned above. Relaxed potential energy scans for all reaction pathway simulations in Figure 5 were performed using mass-weighted differences[47] between two key distances of each reaction pathway. Specifically, C_1–H_4 and H_4–O_1 for C–H bond abstraction, C_1–C_3 and C_2–C_3 for radical ring-expansion, Fe–O_1 and O_1–C_1 for rebound hydroxylation, and O_4–H_5 and H_5–O_4 for O–H bond abstraction were scanned (see Figures 4, 6, 7, 11a, S35-S38, S48-S51, S68-S71, S79-S82, S86-S89, and S93-S96). The QM-cluster models derived from the QM region of Anc3 variant 3 were also investigated to locate all possible C–H bond abstraction pathways (see Sections S1.5.1 and S3.2 (SI)). The QM reaction paths of the diol species **7** for semi-pinacol rearrangement and fragmentation were explored (see Sections S1.5.2 and S7 (SI)). Non-covalent interactions (NCIs) analysis,[48] which reveals hydrogen bonds and van der Waals (vdW) interactions, were performed to explore effects of the first- and second-coordination spheres on mechanistic differences and reaction selectivity (see Figures 4, 7, 11a, S35-S38, S48-S51, S68-S71, S79-S82, S86-S89, and S93-S96).

SET simulations of Anc3 variants 1 and 3 were implemented by combined constrained density functional theory[49]/molecular mechanics (CDFT/MM). CDFT is a useful method for assigning the electron density distribution to achieve a desired charge or spin state.[49] All CDFT/MM simulations were carried out with pDynamo 3.0.9 interfaced with Q-Chem 5.2 for the QM regions

and the CHARMM27 force field for the MM regions.[7c,50] CDFT with the same DFT functional and basis set mentioned above was performed for SET from the substrate radical **4** to the iron fragment (Fe, His211, Asp213, and His270; constrained charge/spin multiplicity = –2/5) in the QM regions. The relaxed potential energy paths of ring-expansion in Figures 9 and S106 were prepared by scanning along distances between C_1–C_3 and C_2–C_3 bonds. The QM-cluster model derived from the QM region of variant 3 was also investigated (see Sections S1.5.3 and S8.2 (SI)).

■ Results

1. Scope of Study. Experimental product ratios for ring-expansion and shunt product formation (**P1**:**P2**) sensitively depend upon Anc3 variants (Figure 1),[8] and these interesting findings motivate the structural and mechanistic simulations of this work. The models focus on four Anc3 variants 1, 2, 3, and 6 with a range of product ratios (from 1.3:1 to 4.9:1). Since mechanisms for the generation of Fe(IV)–oxo have been well established in literature,[6,13] a natural starting point for simulations is **1** + [Fe(IV)=O] (Subsection 2). Reaction paths proceeding from **1** (Subsections 3 and 4) allow study of the origins of the reactivity control (Subsection 5).

The first- and second-coordination spheres around the iron active site comprise the central structural features which guide reactions within the Anc3 variants. The first-coordination sphere ligands binding to the iron are His211, Asp213, His270, succinate, water, and oxo/hydroxyl (see Figures 3, 4, 6, 7, 9, and 11a). This is typical for NHI enzymes which utilize a highly conserved first-coordination environment centered around the iron, composed of a facial triad (two His and Asp (or Glu)) side chains binding to the iron.[14,51] The second-coordination sphere consists of amino acid residues which do not directly bind to the iron but can affect electronic properties through non-covalent interactions,[16] i.e., Arg191, Phe214, Gly215, Phe288, and Asn290/Asp290, including Asp210/Ala210, Arg269, Arg271, and Arg282 which has a salt bridge with the terminal carboxyl group of succinate (Figure S42 and Table S10 (SI)).

2. Structure of 1 + [Fe(IV)=O]. The QM/MM-optimized geometries of **1** + [Fe(IV)=O] for variants 1, 2, 3, and 6 have quintet spin ground states with frontier orbital occupations $\pi^*_{xy}{}^1$ $\pi^*_{xz}{}^1$ $\pi^*_{yz}{}^1$ $\sigma^*_{x2\text{-}y2}{}^1$ $\sigma^*_{z2}{}^0$ (see Figure S33 (SI)). A representative QM/MM-optimized 3D struc-

ture of Anc3 variant 3 is shown in Figure 4 (see Figures S35-S38 (SI) for all variants). Structurally, the Fe–O_1(oxo) distances are 1.61-1.62 Å (Table 1), consistent with the Fe(IV)=O bond distances of the previous studies.[7c,8,15b,c,17f,20a-c,45a-d,46a,b]

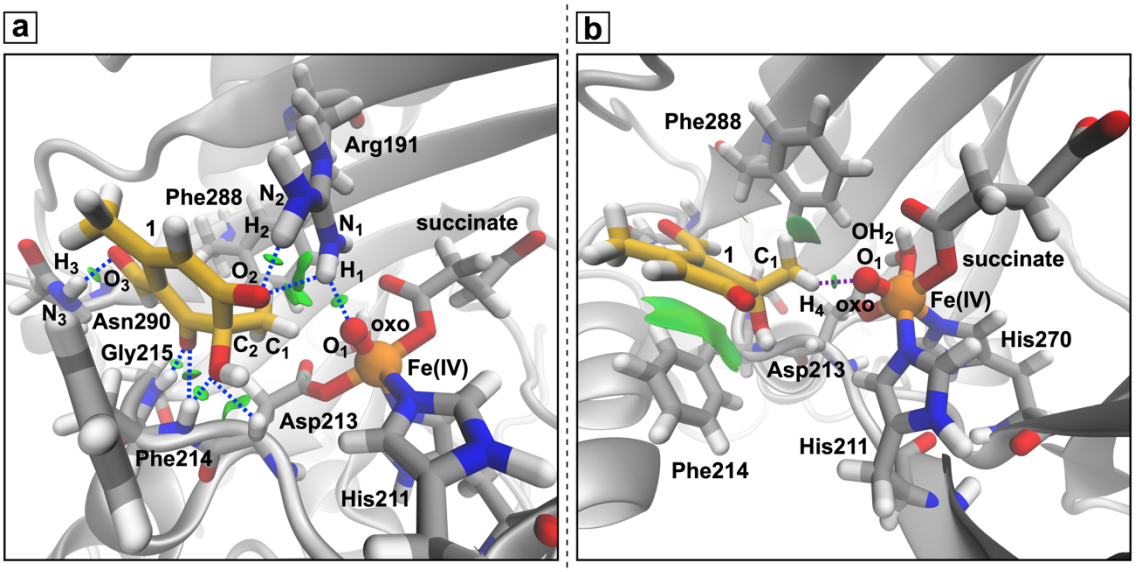

Figure 4. Representative QM/MM-optimized geometry of **1** + [Fe(IV)=O] of Anc3 variant 3: (a) key hydrogen bonds and NCIs of **1**, oxo ligand, and key amino acid residues (Arg191, Asp213, Phe214, Gly215, and Asn290) in the active site and (b) key hydrogen bond (purple dashed line) and NCIs of the adjacent methyl group of **1**, oxo ligand, Phe214, and Phe288. Enzymes shown in gray, **1** in yellow, succinates and key residues in gray, oxo and water ligands in red, and iron(IV) atoms in orange. Hydrogen bonds and NCIs shown in blue dashed lines and green surfaces, respectively. See Tables 1 and S7-S9 for key metrical parameters.

Table 1. Key bond distances and angles of **1** + [Fe(IV)=O] (quintet spin state) in Figure 4.[a]

variant	Fe–O_1 (Å)	C_1–H_4 (Å)	O_1–H_4 (Å)	C_1–H_4–O_1 (°)	Fe–O_1–H_4 (°)	O_1–Fe–H_4 (°)	H_1–O_1 (Å)	N_1–H_1–O_1 (°)	H_3–O_3 (Å)	N_3–H_3–O_3 (°)
1	1.62	1.10	1.93	163.1	133.7	25.3	2.52	111.2	-[b]	-[b]
2	1.61	1.09	2.04	155.3	128.4	29.1	2.42	123.6	1.79	169.5
3	1.61	1.10	2.08	150.9	127.7	29.7	2.40	118.9	1.86	159.1
6	1.62	1.10	2.03	146.4	133.5	26.0	2.34	112.3	1.79	172.5

[a]See Figures S34-S38 (SI) for additional atom labels and key interactions and Tables S7-S9 (SI) for additional metrical parameters. [b]No Asn290 (Asp290 for variant 1).

The substrate **1** is oriented for reaction in the binding pocket through support from non-covalent interactions (Figure 4; see Tables 1 and S7-S9 for key distances and angles). These interactions include π-stacking between **1** and the phenyl ring of Phe214 (Figure 4b), where Phe214 flanks **1** and helps its C_1 methyl group to align with the Fe(IV)=O center.[25] Phe288 further guides the methyl toward the reaction site from the opposite face of Phe214. In addition, Arg191 is a key

residue forming hydrogen bonds to bridge **1** and the oxo ligand (Figure 4a, H_1–O_1 = 2.34-2.52 Å and ∠N_1–H_1–O_1 = 111.2-123.6°). Another key interaction involves the hydrogen bond between Asn290 and **1** (H_3–O_3 = 1.79-1.86 Å and ∠N_3–H_3–O_3 = 159.1-172.5°, except variant 1). Asp213, Phe214, and Gly215 also form hydrogen bond networks with **1**. In all, these position the methyl group of **1** for C–H bond abstraction, with key structural parameters of O_1(oxo)–H_4(**1**) = 1.93-2.08 Å, ∠Fe–O_1–H_4 = 127.7-133.7°, and ∠C_1–H_4–O_1 = 146.4-163.1°. These numerous non-covalent interactions involving first- and second-coordination spheres which combine π-stacking and hydrogen bonds hold the substrate **1** in place for reaction, and will be instrumental in tuning the selectivity of the reaction pathways that will now be delineated. Hydrogen bonds between Arg191, Asn290, and **1** have a significant and direct effect on the reaction selectivity (see Subsection 5).

3. Mechanisms for Tropolone Biosynthesis: Paths 1 and 2. Mechanisms of the conversion of **1** to **P1** and **P2** are summarized in Figure 5 and Tables 2, S11, S15, S25, and S35. Representative 3D structures associated with reaction paths of Anc3 variant 3 are shown in Figures 4, 6, 7, 11a, S37, S50, S70, S81, S88, and S95 (see Sections S2-S6 (SI) for all variants). The first step is C–H bond abstraction of **1** + [Fe(IV)=O] from the adjacent methyl group of **1**. This step occurs through **TS1** with barriers of 19.1-20.2 kcal/mol (quintet spin state, σ pathway) to afford a common primary CH_2-radical intermediate (**4**) and the Fe(III)–OH center at the active site.[7c,8,17f,20,45c,e,i,52] Although this is the rate-determining step, in agreement with the previous studies,[7c,8,17f,20,45c,f,i,52] it does not determine selectivity. Therefore, further details of C–H bond abstraction reaction paths are summarized in Section S3 in SI.

The radical species (**4** + [Fe(III)–OH]; Figures 11a and S70) appearing after C–H bond abstraction is the divergent point from which two transformations likely occur. The radical electronic configuration in [Fe(III)–OH] is $\pi^*_{xy}{}^2\ \pi^*_{xz}{}^1\ \pi^*_{yz}{}^1\ \sigma^*_{x2\text{-}y2}{}^1\ \sigma^*_{z2}{}^0$, and **4** contains an unpaired electron on the primary radical carbon (C_1) (spin density = 0.98; Table 2). As depicted in Figure 5, **4** + [Fe(III)–OH] could proceed to Path 1 (radical ring-expansion) leading to the ring-expansion product **P1** or to Path 2 (rebound hydroxylation) resulting in the shunt product **P2**. Path 1 occurs with attack of the primary radical carbon to the carbonyl carbon, which leads to ring-expansion to

a more stable radical intermediate involving a tertiary radical.[53] This path resembles the mechanism of the Dowd-Beckwith reaction, where ring-expansion of ketones is initiated by primary radicals.[54] Path 2 involves rebound hydroxylation from the Fe(III)–OH to the C_1 carbon, which is a commonplace reaction path for NHI enzymes.[55] The hydroxylated intermediate **7** is likely transformed to **P2** (Figure 2), as supported by experimental observations and simulations of the enzyme in the same protein family, TropC.[7c]

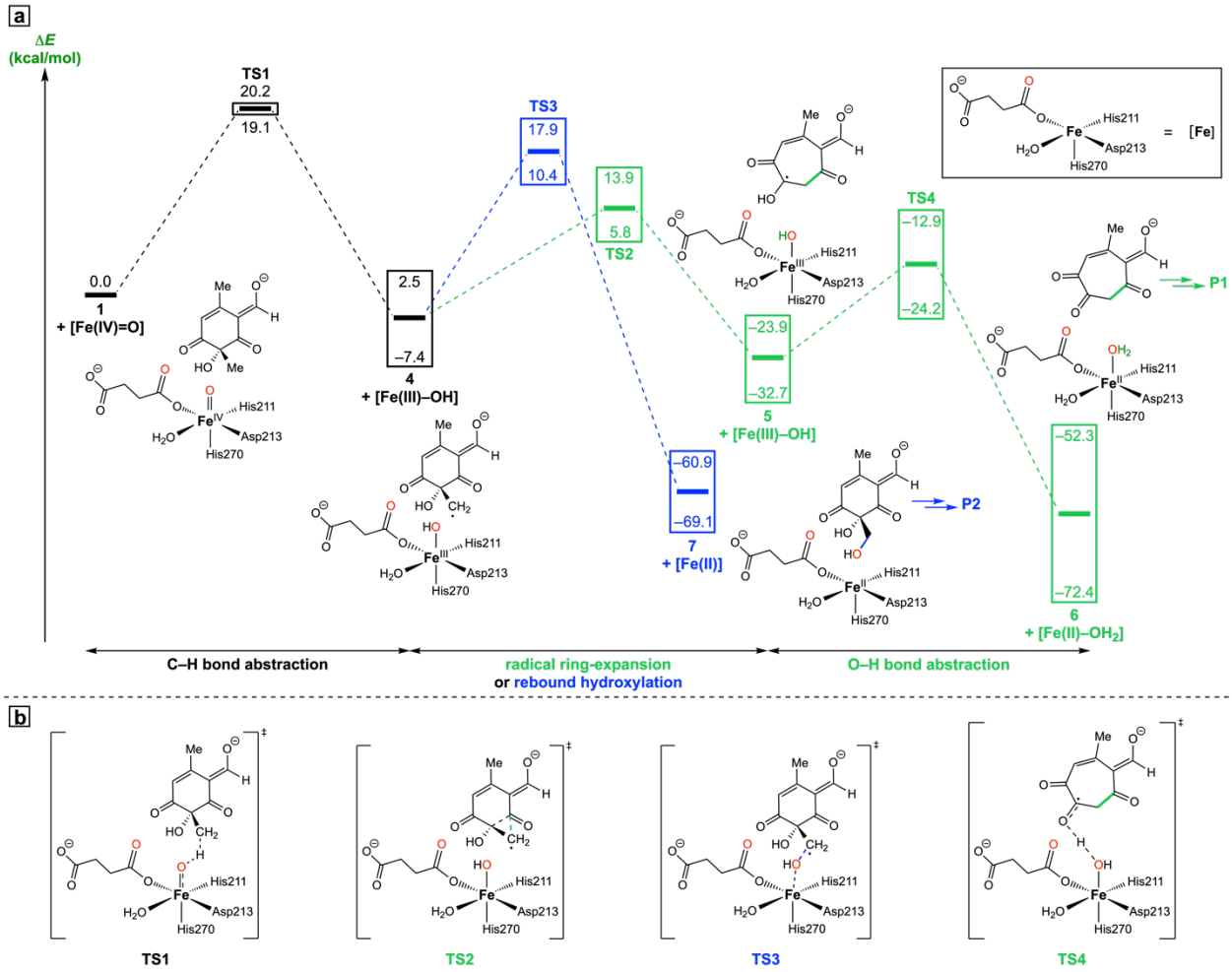

Figure 5. (a) Reaction coordinates (representative of QM/MM models) with energy ranges of Anc3 variants 1, 2, 3, and 6 for tropolone biosynthesis: Paths 1 (radical ring-expansion, green) and 2 (rebound hydroxylation, blue). (b) Transition states **TS1**-**TS4**. See Tables 2, S11, S15, S25, and S35 and Figures S35-S38, S48-S51, S68-S71, S79-S82, S86-S89, and S93-S96 (SI) for energies, key metrical parameters, and enzyme models.

Radical ring-expansion (Path 1) leads to the tertiary radical intermediate **5** with barriers of 11.1-14.4 kcal/mol (**TS2**) across the four Anc3 variants (Table 2). Atomistic details of the ring-expansion from a six- to seven-membered ring are depicted in Figure 6. The ring-expansion begins

with the C_1 approaching the carbonyl carbon (C_3) (nodes 4 and 6; Figures 6b,c), concomitant with the C_2–C_3 bond being elongated (Table S28 (SI)). The reaction path reaches **TS2** at node 8 (Figures 6d, 7a, and S81). The structures of **TS2** are reactant-like with longer C_1–C_3 distances (1.70-1.74 Å) but shorter C_2–C_3 distances (1.59-1.66 Å; Table S26 (SI)). The spin density at the C_1 of **TS2** (0.35) significantly decreases with respect to **4**, but that of the iron (2.87) is relatively constant, indicating the iron is not directly a part of this elementary step (Table 2). The alkoxy radical character of the carbonyl oxygen (O_5) increases along the reaction coordinate (Table S28 (SI)). Just after **TS2**, a transient cyclopropyloxy radical moiety exists (node 11; Figure 6e) with the decrease in the spin density at the O_5 (Table S28 (SI)). Finally, the reaction reaches **5** + [Fe(III)–OH] (Figures 6f and S88) with energies of –21.0 to –35.2 kcal/mol (Table 2), compared to its starting point, **4** + [Fe(III)–OH]. The spin density at the tertiary radical carbon (C_2) increases to 0.55 along with the disappearance of the spin densities at the C_1 and O_5 (Table 2).

Table 2. Relative electronic energies (ΔE) and spin densities of key atoms of species and transition states in Figure 5. Spin densities are averages across Anc3 variants 1, 2, 3, and 6. Tables S53-S61 (SI) contain specific values for each variant.

species	ΔE (kcal/mol)				spin density		
	variant 1	variant 2	variant 3	variant 6	Fe[a]	C_1[a]	C_2[a]
1 + [Fe(IV)=O]	0.0	0.0	0.0	0.0	3.23	0.00	0.00
TS1	19.3	19.1	20.2	20.0	3.70	–0.16	0.00
4 + [Fe(III)–OH]	–2.9	2.5	–7.4	–0.1	2.88	0.98	–0.04
TS2	11.5	13.9	5.8	11.0	2.87	0.35	0.11
TS3	13.7	17.9	10.4	15.4	3.20	0.89	–0.04
5 + [Fe(III)–OH]	–23.9	–32.7	–27.5	–28.6	2.85	–0.05	0.55
7 + [Fe(II)]	–64.4	–65.6	–60.9	–69.1	3.83	0.00	0.00
TS4	–12.9	–24.2	–17.4	–18.7	2.91	–0.05	0.56
6 + [Fe(II)–OH_2]	–71.2	–72.4	–52.3	–56.5	3.81	0.00	0.00

[a]See Figures 4, 6, 7, 11a, S35-S38, S48-S51, S68-S71, S79-S82, S86-S89, and S93-S96 for atom labels.

Figures 6, 7a, and S81 show that Arg191, Asp213, Phe214, Gly215, and Asn290 remain in hydrogen bonding configurations as ring-expansion proceeds. In addition to hydrogen bonding with the substrate radical, Arg191 also interacts with the hydroxyl ligand, providing a stabilizing effect that helps ring-expansion outcompete rebound hydroxylation (Path 2; Figures 7b and S95).

Altogether, these residues not only orient the substrate **1** for C–H bond abstraction and intermediate **4** for ring-expansion, one of them also contributes to slowing down the otherwise-expected re-bound hydroxylation reaction (see Subsection 5 for further details).

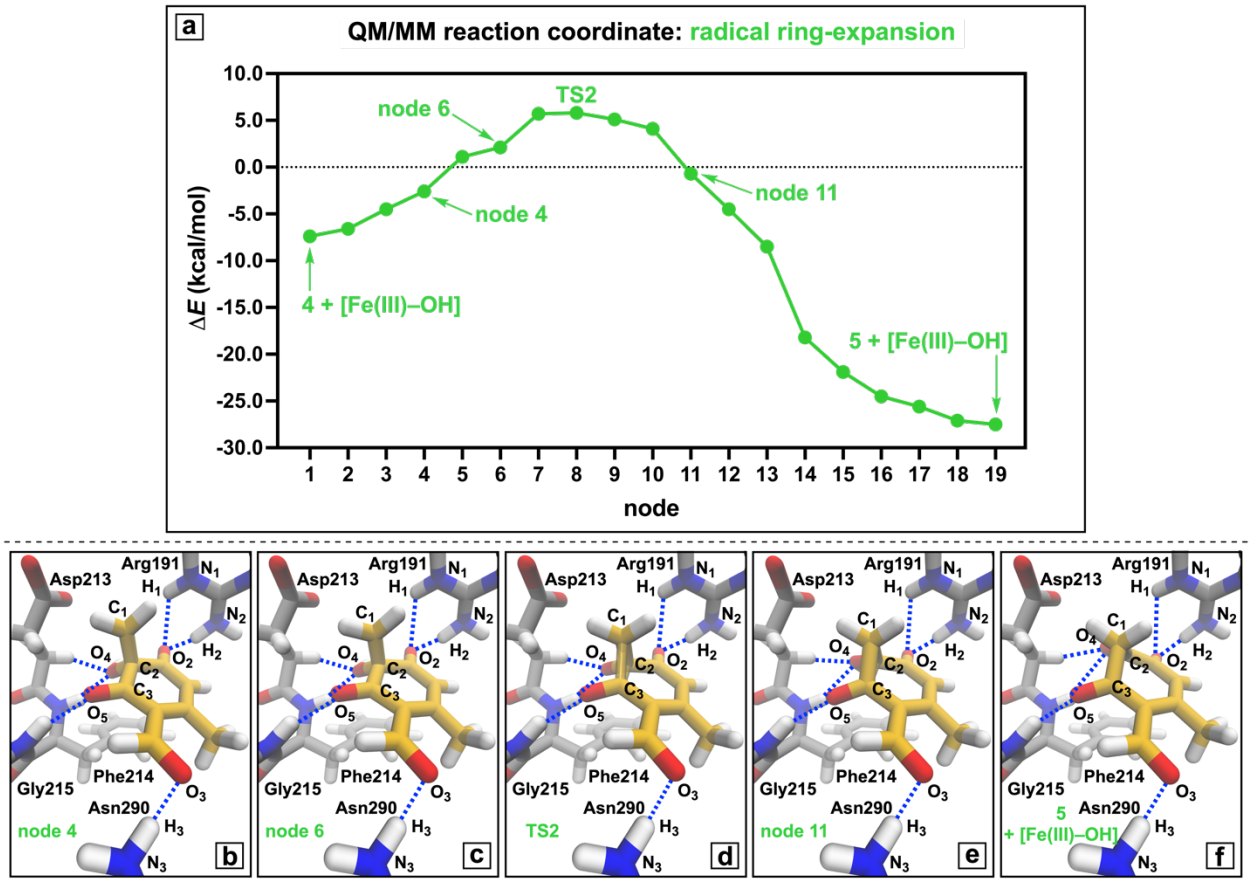

Figure 6. (a) Representative reaction coordinate for radical ring-expansion (Path 1) of Anc3 variant 3. The corresponding 3D QM/MM-optimized geometries: (b) node 4, (c) node 6, (d) **TS2**, (e) node 11, and (f) **5** + [Fe(III)–OH]. Enzyme structures and the Fe(III)–OH centers are omitted for clarity. Intermediates and key amino acid residues shown in yellow and gray, respectively. Hydrogen bonds shown in blue dashed lines. See Figures 11a and S70 for **4** + [Fe(III)–OH], Figures 7a and S88 for the alternative views of **TS2** and **5** + [Fe(III)–OH], respectively, and Tables S22, S23, and S25-S30 (SI) for energies and key metrical parameters.

For Path **1** to reach **P1**, radical termination through O–H bond abstraction from **5** + [Fe-(III)–OH] must be accessible. This step is viable with the barriers of 8.5-11.0 kcal/mol (**TS5**) to afford the tropolone tautomer **6** + [Fe(II)–OH_2] (Figure S88 (SI) and Tables 2 and S29-S34). The spin density at the iron of **6** + [Fe(II)–OH_2] increases to 3.81 from 2.85 of **5** + [Fe(III)–OH] (Table 2), consistent with the change of the oxidation state from Fe(III) to Fe(II). Here, Fe(II) has the electronic configuration $\pi^*_{xy}{}^2\ \pi^*_{xz}{}^1\ \pi^*_{yz}{}^1\ \sigma^*_{x2\text{-}y2}{}^1\ \sigma^*_{z2}{}^1$, and the spin density at the C_2 of **6** has disappeared (Table 2). The energies of **6** + [Fe(II)–OH_2] are significantly lower than those of **4** +

[Fe(III)–OH] (–52.3 to –72.4 kcal/mol vs. –7.4 to 2.5 kcal/mol; Table 2), due to the strong oxidative thermodynamical driving force. Species **6** tautomerizes and is protonated to produce **P1** (Figure 2) to complete the formation of the tropolone product. In all, Path 1 starting from **4** + [Fe(III)–OH] is viable to reach the tropolone product **P1**.

Rebound hydroxylation (Path 2) competes with radical ring-expansion, with barriers of 15.4-17.7 kcal/mol (**TS3**; Figures 7b and S95) to afford the diol intermediate **7** + [Fe(II)]. The structures of **TS3** are reactant-like, in which the C_1(**1**)–O_1(OH) distances are longer than the Fe–O_1(OH) distances (2.53-2.70 Å vs. 2.07-2.19 Å; ∠Fe–O_1–C_1 = 138.3-146.7°; Table S36 (SI)), in agreement with previous studies of related hydroxylation of NHI enzymes and iron biomimetic complexes.[17f,56] The spin density at the C_1 decreases to 0.89 at **TS3** (vs. 0.98 for **4** + [Fe(III)–OH]) and disappears for species **7** (Table 2), indicating quenching of the radical center. Subsequently, **7** + [Fe(II)] has been hypothesized to proceed via two possible pathways: semi-pinacol rearrangement leading to **P1** or fragmentation resulting in **P2** (Figure 2).

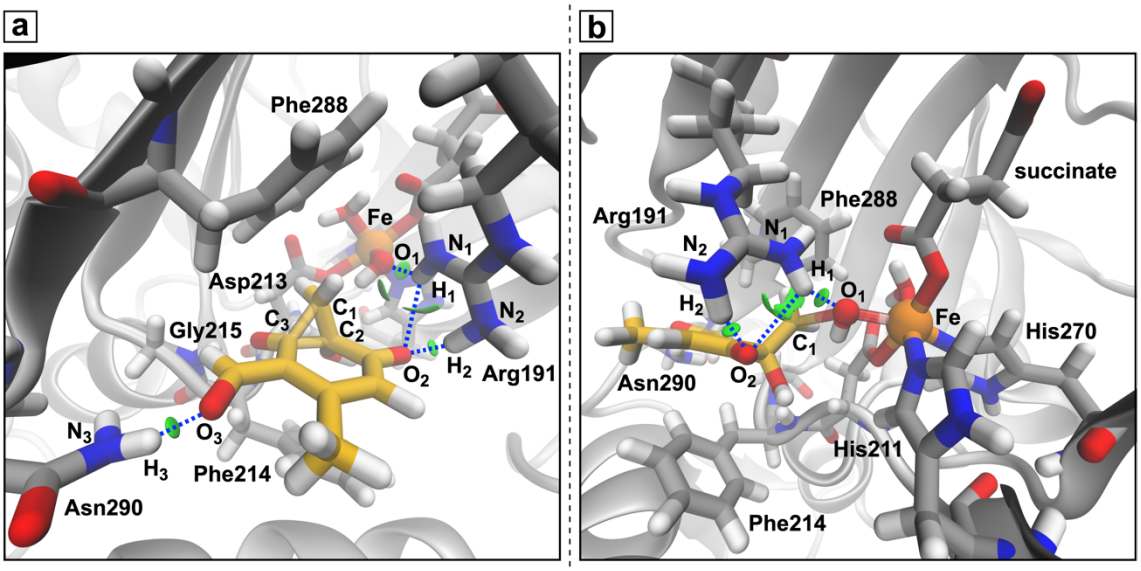

Figure 7. Representative 3D QM/MM-optimized geometries of Anc3 variant 3 showing key hydrogen bonds and NCIs between the intermediates and amino acid residues in the active site: (a) **TS2** and (b) **TS3**. Enzymes shown in gray, intermediates in yellow, succinates and key residues in gray, oxo, hydroxyl, and water ligands in red, and iron atoms in orange. Hydrogen bonds and NCIs shown in blue dashed lines and green surfaces, respectively. See Figures S70, S81, and S95 (SI) for additional atom labels and key interactions and Tables S26-S28, S36, and S37 (SI) for key metrical parameters.

Figure 8 gives an overview of the two pathways from **7** leading to **P1** or **P2** (see also Section S7 (SI)). The barrier of the former is much higher than that of the latter (56.5 kcal/mol vs.

22.9 kcal/mol). This insurmountable barrier of semi-pinacol rearrangement is consistent with the computational studies of TropC[7c] and ring-expansion mechanisms of *ortho*-dearomatized phenols.[57] In all, these imply that the dominant pathway from **7** is fragmentation and concomitant rearomatization and protonation to afford **P2** (Figure 2), and the high barriers of semi-pinacol rearrangement preclude rebound hydroxylation as a pathway to ring-expansion. However, the reason why fragmentation is more favorable than semi-pinacol rearrangement deserves further explanation.

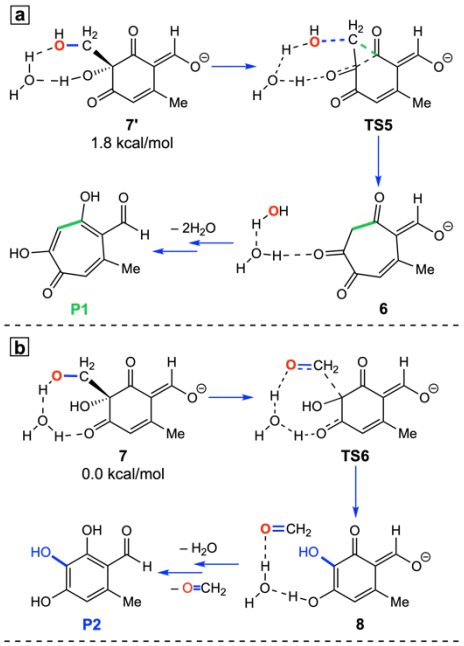

Figure 8. QM reaction paths for (a) semi-pinacol rearrangement and (b) fragmentation with (c) the energies associated with the distortion/interaction model. The energies are relative to **7** + H_2O (fragmentation).

The distortion/interaction model[58] was applied to provide insights regarding origins of the insurmountable barriers of semi-pinacol rearrangement (see Section S1.5.5 (SI)). This approach relates the distortion energy, ΔE_{dis}, which measures the energetic cost for distorting the geometry of **7** + H_2O into that of **TS5** or **TS6**, to the interaction energy, ΔE_{int}, which measures the energy release by taking the distorted **7** and H_2O components into the geometry of **TS5** or **TS6**. As summarized in Figure 8, the $\Delta E_{dis\text{-}7}$, $\Delta E_{dis\text{-}H2O}$, and ΔE_{int} of **TS5** are significantly larger than

those of **TS6** (138.0, 81.6, and –163.0 kcal/mol vs. 85.7, 75.1, and –137.9 kcal/mol). The ΔE_{int} values are not large enough in magnitude to overcome the high ΔE_{dis} for **TS5**. The high ΔE_{dis} of semi-pinacol rearrangement can be traced to asynchronicity of **TS5**, where the C–C and C–OH bonds must break before the new C–C bond starts to form (distances 1.83, 2.10, and 2.15 Å at **TS5**, see Figures S100 and S101 and Table S40 (SI)). Fragmentation occurs with much less distortion, consistent with the ease of formaldehyde loss from the six-membered ring of **7** (Figures S104 and S105 and Table S42 (SI)). Thus, the significant distortion of the diol geometry (**7**) of semi-pinacol rearrangement with respect to fragmentation likely leads to higher E_a (56.5 kcal/mol vs. 22.9 kcal/mol). In other words, the hydroxyl group is a poor leaving group, limiting the viability of semi-pinacol rearrangement.[59] Altogether, they support the infeasibility of **7** leading to **P1**.

The QM/MM simulations indicate that barriers of radical ring-expansion through Path 1 are lower than those of rebound hydroxylation through Path 2 (11.1-14.4 kcal/mol vs. 15.4-17.7 kcal/mol; Figure 5 and Table 2). This finding makes product **P1** more likely to appear than **P2**, consistent with the experimental selectivity in Figure 1c. However, there may be another competitive channel starting from **4** + [Fe(III)–OH], as this radical species can perform a variety of transformations.[5a-c,6-8,11,15,17] One possible pathway involving SET from the radical intermediate to the Fe(III)–OH center may drive the ring-expansion to afford **P1**.[15,17] Therefore, the possibility of a third pathway through SET was considered next.

4. Alternative Mechanism: Path 3. Product **P1** forms alongside conversion of Fe(III) to Fe(II), providing an oxidative driving force that may enable SET. Therefore, electron transfer from the substrate radical **4** to the Fe(III)–OH center could facilitate polar, cationic ring-expansion. If electron transfer were viable, ring-expansion would occur quickly due to the formation of an unstable cationic substrate, and then Path 3 might be faster than Path 1.[15b,c] Accordingly, SET was explored for Anc3 variants 1 and 3 as an alternative reaction path for generating **P1** (see Figure 9 for variant 3 and Figure S106 (SI) for variant 1).

SET from the radical substrate **4** to the Fe(III)–OH center could form the primary carbocation/zwitterionic species **9** and the Fe(II)–OH center (Figures 2, 9, and S106). Simulations of the

SET process indicate an increase in spin densities at the iron from 2.86-2.89 of **4** + [Fe(III)–OH] to 3.71-3.72 of **9** + [Fe(II)–OH] and a decrease in spin densities at the C_1 from 0.98 of the former to 0.05-0.09 of the latter (Figures 9b and S106 and Tables 2, S55, and S62). This confirms an electron transfer from the CH_2 radical to the empty σ^*_{z2} orbital on the Fe(III)–OH center. Thus, the electronic configuration of **9** + [Fe(II)–OH] is $\pi^*_{xy}{}^2\ \pi^*_{xz}{}^1\ \pi^*_{yz}{}^1\ \sigma^*_{x2\text{-}y2}{}^1\ \sigma^*_{z2}{}^1$.

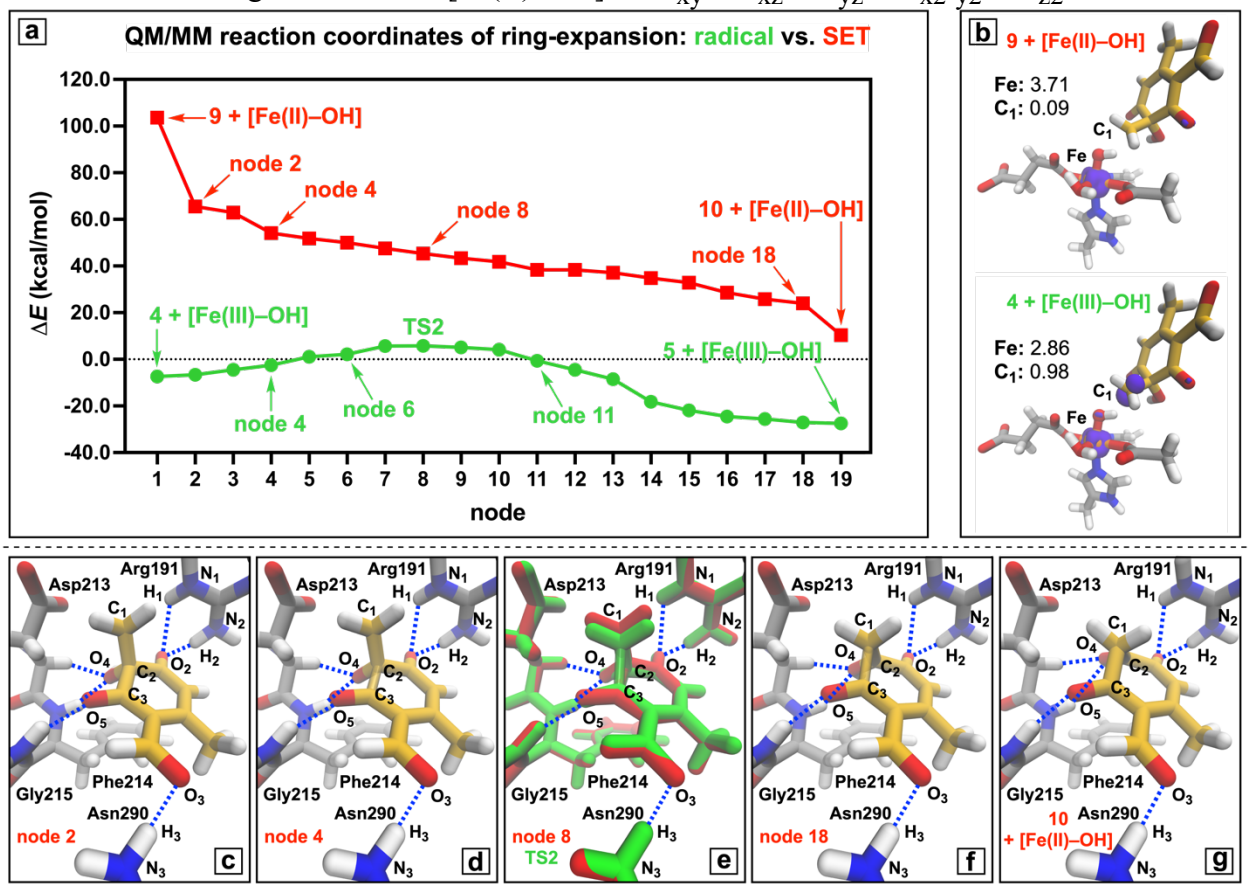

Figure 9. (a) Representative reaction coordinates for radical (Path 1, green) and SET (Path 3, red) ring-expansion of Anc3 variant 3. (b) Spin density plots (purple) at the iron and C_1 atoms in the QM regions of **4** + [Fe(III)–OH] and **9** + [Fe(II)–OH]. The corresponding 3D QM/MM-optimized geometries of species associated with Path 3: (c) node 2, (d) node 4, (e) overlaid **TS2** (radical, green) and node 8 (SET, red), (f) node 18, and (g) **10** + [Fe(II)–OH]. Enzyme structures and the Fe(II)–OH centers are omitted for clarity. Intermediates shown in yellow, and succinates and key amino acid residues in gray. Hydrogen bonds shown in blue dashed lines. See Figures S108 and S110 (SI) for schematic reaction coordinate and the alternative view of **10** + [Fe(II)–OH] and Tables S44-S46 (SI) for energies and key metrical parameters.

The polar ring-expansion could take place from **9** + [Fe(II)–OH] to form the more stable tertiary carbocation/zwitterionic species **10** + [Fe(II)–OH], which subsequently undergoes O–H bond abstraction to afford the tropolone tautomer **6′** + [Fe(II)–OH_2] (Figures 2, S107, and S108). The ring-expansion through the SET pathway begins with the breaking C_2–C_3 bond and subse-

quent C_1–C_3 bond forming (Figure 9), which is distinct from the mechanism of the radical pathway (Figure 6). Although Path 3 could in principle result in the ring-expansion, being an all-downhill pathway from **9** + [Fe(II)–OH] to **10** + [Fe(II)–OH], the vertical energy costs of SET from **4** + [Fe(III)–OH] to reach **9** + [Fe(II)–OH] are over 100 kcal/mol and entirely unlikely (Figures 9a and S106). In addition, SET is infeasible to occur along the reaction coordinate as the energies of species associated with the SET pathway are over 31 kcal/mol higher than those of the radical pathway (Figures 9a and S106). Therefore, SET is not viable in the Anc3 active sites, at least for species **4** that is relevant to the present study (see Section S8 (SI) for further details).

5. Origins of Reaction Selectivity between P1 and P2. As summarized in Figure 10, the QM/MM models provide a good description of the reaction selectivity across the four Anc3 variants, in which the product ratios between **P1** and **P2** are governed by their relative rates of the selectivity-determining steps. Specifically, the computed energy gaps ($\Delta E_a = E_a$(**TS3**) – E_a(**TS2**)) between radical ring-expansion and rebound hydroxylation trend with their product ratios. For example, the ΔE_a value of variant 1 is lower than that of variant 2 (2.2 kcal/mol vs. 3.9 kcal/mol), consistent with the product ratios between **P1** and **P2** (1.3:1 (variant 1) vs. 2.8:1 (variant 2)). As a result, we anticipate that the QM/MM models contain the necessary physical interactions that tune the reaction selectivity between radical ring-expansion and rebound hydroxylation.

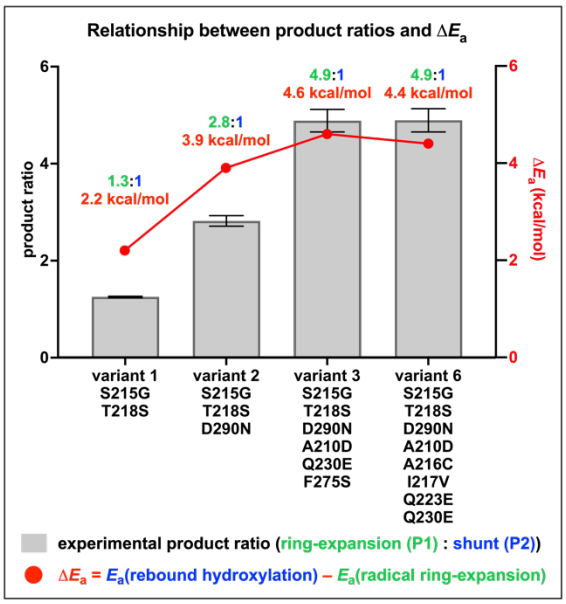

Figure 10. Relationship between product ratios and ΔE_a (kcal/mol) of Anc3 variants 1, 2, 3, and 6.

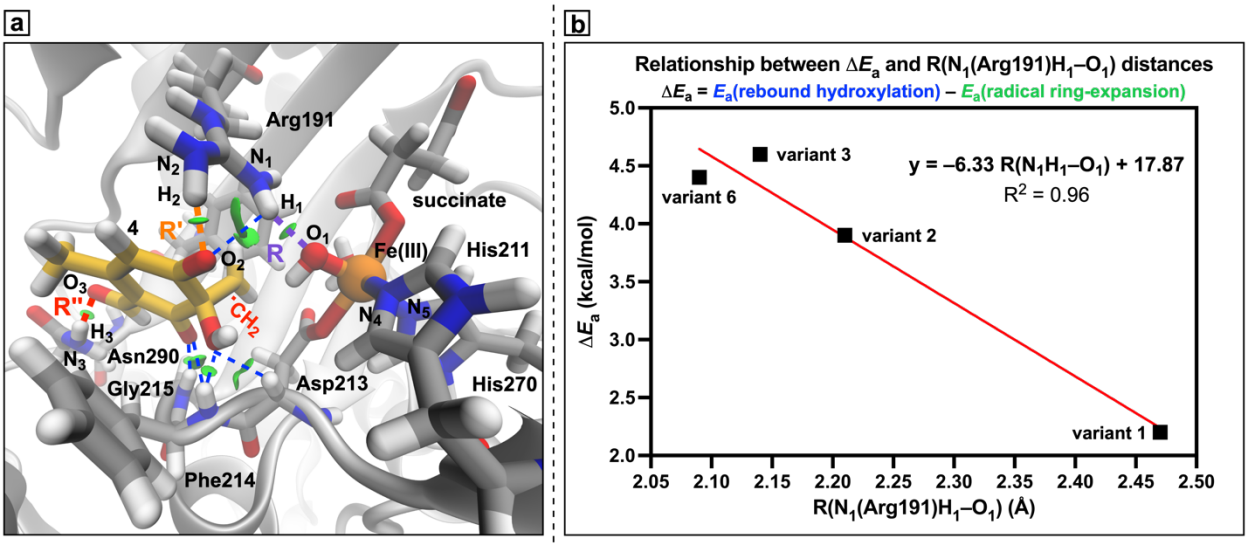

Figure 11. (a) Representative 3D QM/MM-optimized geometry of **4** + [Fe(III)–OH] of Anc3 variant 3 showing key hydrogen bonds: N_1(Arg191)H_1 and hydroxyl ligand (R; purple dashed line), N_2(Arg191)H_2 and O_2(**4**) (R′; orange dashed line), and N_3(Asn290)H_3 and O_3(**4**) (R″; red dashed line). (b) Relationship between ΔE_a (kcal/mol) and R(N_1-(Arg191)H_1–O_1) distances (Å). Enzyme shown in gray, **4** in yellow, succinate and key amino acid residues in gray, hydroxyl and water ligands in red, and iron(III) atom in orange. Other hydrogen bonds and NCIs shown in blue dashed lines and green surfaces, respectively. See Tables 2, 3, S22, and S23 and Figures 10 and S68-S71 for energies, key metrical parameters, and enzyme models.

Table 3. Key bond distances and angles of **4** + [Fe(III)–OH] in Figure 11a.[a]

variant	H_1–O_1[b] (Å)	N_1–H_1–O_1[b] (°)	H_1–O_2 (Å)	N_1–H_1–O_2 (°)	H_2–O_2[c] (Å)	N_2–H_2–O_2[c] (°)	H_3–O_3[d] (Å)	N_3–H_3–O_3[d] (°)	Fe–N_4[e] (Å)	Fe–O_1[f] (Å)
1	2.47	110.0	2.23	134.2	1.96	139.0	-[g]	-[g]	2.28	1.79
2	2.21	131.3	2.59	129.2	1.83	154.5	1.81	169.4	2.26	1.79
3	2.14	132.2	2.53	115.3	1.70	158.1	1.78	163.6	2.06	1.78
6	2.09	123.1	2.77	120.6	1.79	151.1	1.77	173.6	2.16	1.78

[a]See Figures S68-S71 (SI) for additional atom labels and Tables S22 and S23 (SI) for additional metrical parameters. [b]Defined as R(N_1(Arg191)H_1–O_1) and ∠N_1(Arg191)–H_1–O_1. [c]Defined as R′(N_2(Arg191)H_2–O_2) and ∠N_2(Arg191)–H_2–O_2. [d]Defined as R″(N_3(Asn290)H_3–O_3) and ∠N_3(Asn290)–H_3–O_3. [e]Defined as Fe–N_4(His211). [f]Defined as Fe–O_1(OH). [g]No Asn290 (Asp290 for variant 1).

Given that the radical species **4** + [Fe(III)–OH] connects to the selectivity-determining steps (Path 1 vs. Path 2) that lead to **P1** and **P2**, origins of the reaction selectivity can be described through analysis of **4** + [Fe(III)–OH]. Figure 11 shows ΔE_a is significantly associated with hydrogen bond distances (R(N_1(Arg191)H_1–O_1)) between Arg191 and the hydroxyl ligand on the Fe(III)–OH center in **4** + [Fe(III)–OH], highlighted by the NCI plots. In other words, stronger hydrogen bonding of Arg191 to the Fe(III)–OH center results in higher ΔE_a. To illustrate, the higher ΔE_a of variant 2 (3.9 kcal/mol) with respect to variant 1 (2.2 kcal/mol) corresponds to that the R(N_1-

(Arg191)H_1–O_1) distance of the former is shorter than that of the latter (2.21 Å vs. 2.47 Å), with N_1–H_1–O_1 angles of 131.3° and 110.0°, respectively, indicating better alignment of the hydrogen bonds as well.

Figure 11b also shows that the four variants establish a nearly linear relationship between ΔE_a and R(N_1(Arg191)H_1–O_1) distances ($R^2 \sim 0.96$). This is consistent with the hydroxyl ligand being supported as a ligand to iron by a hydrogen bond, making it more difficult to transfer to the radical center of **4**. When the hydroxyl prefers to stay in place on the iron, radical ring-expansion is expected to be the dominant pathway (see Section S9 (SI) for further details).

What determines the differences in the hydrogen bond strength between Arg191 and the hydroxyl ligand in **4** + [Fe(III)–OH] across the four Anc3 variants? These could be analyzed through the key residue 290, distinguishing variant 1 from the rest. Asn290 of variants 2, 3, and 6 can hydrogen bond with the O_3 of **4** (R″(N_3(Asn290)H_3–O_3), 1.77-1.81 Å; Figures 11a and S68-S71 and Table 3), whereas Asp290 of variant 1 cannot. This interaction significantly changes the alignments between Arg191 and **4**, as evidenced by the different hydrogen bond distances (R′(N_2-(Arg191)H_2–O_2)) between Arg191 and the O_2 of **4** (Figures 11a and S68-S71). The R′(N_2(Arg-191)H_2–O_2) distances of variants 2, 3, and 6 are shorter than that of variant 1 (1.70-1.83 Å vs. 1.96 Å) with N_2(Arg191)–H_2–O_2 angles of 151.1-158.1° vs. 139.0° (Table 3). Since Arg191 hydrogen bonds with the hydroxyl ligand as well as **4**, the shorter R′(N_2(Arg191)H_2–O_2) distances of variants 2, 3, and 6 in turn afford their shorter R(N_1(Arg191)H_1–O_1) distances with respect to variant 1. Altogether, the alignments between Arg191 and **4**, oriented by the existence of Asn290, control the R(N_1(Arg191)H_1–O_1) distances.

Variant 3 has a predicted slightly higher selectivity for ring-expansion than the hydrogen bonding of Arg191 would suggest (ΔE_a = 4.6 kcal/mol, **P1**:**P2** ratio = 4.9:1, and R(N_1(Arg191)H_1–O_1) = 2.14 Å; Figures 10, 11 and S70 and Table 3), and this might originate from the two key mutations in the active site. Compared to variant 2, variant 3 modifies Ala210 to Asp210 and Gln-230 to Glu230 (Figure S78 (SI)). These changes alter His211 orientations (see Figure 12 and Section S4 (SI) for further details), which makes the Fe–N_4(His211) distance of **4** + [Fe(III)–OH] of

variant 3 significantly shorter than those of variants 1 and 2 (2.06 Å vs. 2.28 and 2.26 Å; Figures 11a and S68-S70 and Table 3). The shorter Fe–N_4(His211) distance of variant 3 indicates the stronger σ- and π-donation from the coordinated N_4(His211) atom to acceptor orbitals ($\sigma^*_{z2}{}^0$ and $\pi^*_{xz}{}^1$) on the iron. The stronger coordination of His211 then weakens electron donation from the N_5(His270) ligand to the same shared acceptor orbitals ($\sigma^*_{z2}{}^0$ and $\pi^*_{xz}{}^1$) on the iron and the corresponding $\sigma^*(d_{z2}(Fe)\text{-}p_z(OH))$ and $\pi^*(d_{xz}(Fe)\text{-}p_x(OH))$ orbitals.[60] This point regarding coordination strength will be quantified in the next paragraph.

Table 4. Ligand binding energies[a] (kcal/mol) of His211, His270, and the hydroxyl (OH) ligand to the iron center of Anc3 variants 1, 2, and 3 in Figure 11a.

variant	binding energy of His211	binding energy of His270	binding energy of OH ligand
1	21.8	34.2	135.8
2	20.8	32.8	134.4
3	23.9	30.6	152.9

[a]Single point calculations at the level of unrestricted B3LYP-D3BJ/6-31G(d).

The strengths of interaction of N_4(His211) and N_5(His270) to the iron center were evaluated by computing the ligand binding energies (see Section S1.5.4 (SI)). As shown in Table 4, the binding energies of His211 to the iron are as follows: 20.8 kcal/mol (variant 2) ~ 21.8 kcal/mol (variant 1) < 23.9 kcal/mol (variant 3). Conversely, the binding energies of His270 to the iron are as follows: 32.8 kcal/mol (variant 2) ~ 34.2 kcal/mol (variant 1) > 30.6 kcal/mol (variant 3). Since His270 is *trans* to the hydroxyl ligand, the weaker *trans*-influence[61] from His270 affords the slightly stronger Fe(III)–OH bond in variant 3, as evidenced by the higher binding energy of the hydroxyl ligand to the iron (152.9 kcal/mol vs. 134.4-135.8 kcal/mol; Table 4). Furthermore, this influence can cooperate with the interaction between Arg191 and the Fe(III)–OH center to alter the hydroxyl transfer to the CH_2 radical center as the binding energies of the hydroxyl ligand also contain the components of the Arg19–OH interaction (see Section S1.5.4 (SI)).[62] Altogether, variations in ligand binding to the iron center predominantly affect the hydroxylation barriers (Path 2), but have little effect on radical ring-expansion (Path 1). These results suggest that the mutated

Asp210 in the second-coordination sphere of variant 3 promotes radical ring-expansion, at least in terms of relative rates (further details of the product ratio between **P1** and **P2** of variant 6 are discussed in Section S4 (SI)).

■ Discussion

NHI enzymes catalyze different transformations compared to analogous biomimetic complexes and homogenous catalysts, even though they have the same iron center and first-coordination spheres.[16] The enzyme environment is therefore critical to positioning substrates and oxidants for site- and chemoselective activation of substrates. Channels that may be active outside the enzymes are prohibited by non-covalent interactions in the secondary-coordination spheres, even though the iron center is capable of performing these alternative steps.[16] Similarly, our QM/MM models reveal the particular interactions that dictate substrate positioning, mechanistic differences, and influence over reaction selectivity (radical ring-expansion vs. rebound hydroxylation) across the four Anc3 variants. The central findings – how various non-covalent interactions associated with first- and second-coordination spheres hold the substrate radical **4** in place for reaction and control the product ratios between **P1** and **P2** are embodied in Figure 12.

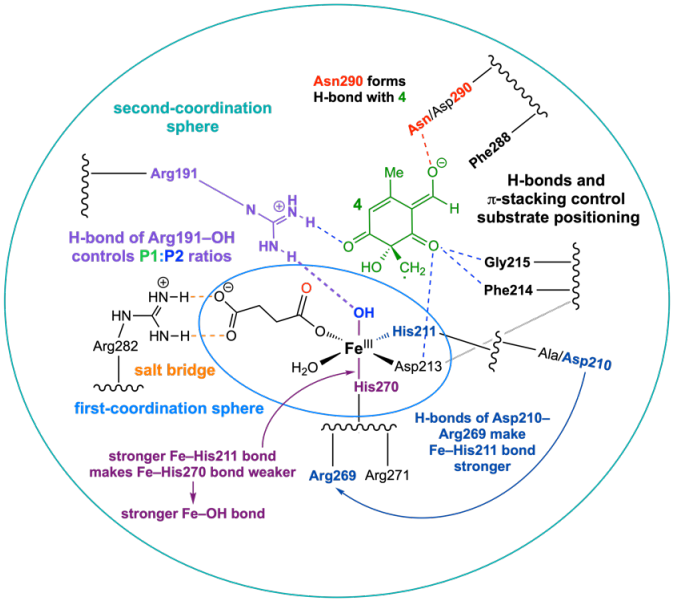

Figure 12. Key non-covalent interactions of **4** + [Fe(III)–OH] altering product ratios between **P1** and **P2**.

One interesting parameter showing that these non-covalent interactions alter substrate positioning is the oxo–iron–H(**1**) angle of **1** + [Fe(IV)=O] (Figures 4 and S35-S38). The QM/MM

models show that the oxo–iron–H(**1**) angles of the four Anc3 variants are consistent with one another ($\angle O_1$–Fe–H_4, 25.3-29.7°; Table 1), and the O_1–Fe–H_4, Fe–O_1–H_4, and Fe–O_1–C_1 angles and [Fe]O_1–C_1 distances of **4** + [Fe(III)–OH] are also respectively comparable (24.3-24.7°, 105.7-106.6°, 129.3-132.2°, and 2.88-2.97 Å; Table S22 (SI)). According to the QM/MM models (Figures 4, 7b, 11a, S35-S38, S68-S71, and S93-S96), the alignments of the substrate in **1** + [Fe(IV)=O] remain consistent in **4** + [Fe(III)–OH], showing that the initial orientation of the substrate for C–H bond abstraction also influences the likelihood of rebound hydroxylation. The [Fe]O_1–C_1 distances may not be the most favorable for rebound hydroxylation, allowing ring-expansion to preferentially occur (with little dependence on the iron center for that step).[17f] Thus, the oxo–iron–H(**1**) angles of **1** + [Fe(IV)=O] as set by the enzymes can be a helpful hint for predicting preferred reaction paths. This finding is in agreement with a previous computational study of NHI/α-KG-dependent halogenases and hydrogenases by Kulik and co-workers.[45i]

The QM/MM models emphasize that Arg191′s hydrogen bond with the Fe(III)–OH center in **4** + [Fe(III)–OH] slows the hydroxyl ligand for transfer to the CH_2 center (Figures 7b, 11a, S68-S71, and S93-S96). This observation is consistent with a computational study of the naphthyridinomycin biosynthesis enzyme I (NapI) activation of L-Arg by de Visser and co-workers.[17f] Both Anc3 and NapI are in a NHI dioxygenase family and share the common mechanistic details, at least for C–H bond abstraction being rate-determining step and rebound hydroxylation being relatively inhibited. In NapI, hydrogen bonds between the hydroxyl ligand and nearby Glu and Lys residues inhibit hydroxyl transfer to L-Arg. Therefore for both Anc3 and NapI, the desired pathway (ring-expansion or desaturation) is enhanced by hydrogen bonding interactions that slow down a competing pathway.

Finally, salt bridges between the terminal carboxylate group of α-KG or succinate and an Arg residue have been shown to affect substrate positioning.[16a] In Anc3 variants, however, this interaction between first- and second-coordination spheres does not obviously relate to the reaction selectivity (Figure S42 and Table S10 (SI)). At the same time, our QM/MM models suggest hydrogen bond networks in the second-coordination sphere are important for selectivity, specifically

through Arg269 altering His211 orientations and His270 bindings (see Figures 12 and Section S4 (SI)). These intercoordination sphere effects alter the Fe(III)–OH bond strengths of **4** + [Fe(III)–OH] and are important for tuning rebound hydroxylation barriers (see Subsection 5 in the Results section).

■ Conclusions

This combined MD and QM/MM study reveals a detailed mechanistic analysis of the reaction of **1** within Anc3 enzymes, showing how this cyclohexadienone can transform through two key pathways. The radical intermediate **4** + [Fe(III)–OH] bifurcates into dominant radical ring-expansion (Path 1) leading to **P1** and little rebound hydroxylation (Path 2) resulting in **P2**. The energy gaps (ΔE_a) between radical ring-expansion and rebound hydroxylation nicely correspond to the experimentally observed product ratios between **P1** and **P2** (Figure 10). This study reveals how the hydrogen bond between Arg191 and the Fe(III)–OH center of **4** + [Fe(III)–OH] contributes to the reaction selectivity (Subsection 5 in the Results section). Furthermore, first- and second-coordination sphere effects can be simultaneously employed to further tune the Fe(III)–OH bond strengths of **4** + [Fe(III)–OH] (Subsection 5 in the Results section). In all, this study improves understanding of how changes in just a few amino acid residues of Anc3 variants resulted in substantial shifts in the predominant reaction pathway (Figure 1c), and therefore is valuable information for future enzyme engineering, rational reaction design, and mechanistic inquiry.

■ ASSOCIATED CONTENT

Supporting Information. Additional computational details, key enzyme structures, energy profiles of additional QM/MM and QM reaction paths, analysis of the Arg191–OH hydrogen bond, key metrical data, and spin densities. This material is available free of charge via the Internet at http://pubs.acs.org.

Optimized structure files (xyz) of the QM regions of the QM/MM models and QM calculations.

■ AUTHOR INFORMATION

Corresponding Author

*E-mail: paulzim@umich.edu.

Complete contact information is available at https://pubs.acs.org/doi/10.1021/acscatal.4cxxxxx.

Notes

The authors declare no competing financial interest.

ORCID

Taveechai Wititsuwannakul: 0000-0002-3752-3089

Kevin C. Skinner: 0000-0001-8591-1169

Joshua A. Kammeraad: 0000-0003-0386-7198

Alison R. H. Narayan: 0000-0001-8290-0077

Paul M. Zimmerman: 0000-0002-7444-1314

■ ACKNOWLEDGEMENT

The authors thank the U.S. National Institutes of Health (R35-GM128830) for support, and Prof. Michael B. Hall and Mr. Azam Hussain for helpful discussions.

■ References

(1) Puig, S.; Ramos-Alonso, L.; Romero, A. M.; Martinez-Pastor, M. T. The elemental role of iron in DNA synthesis and repair. *Metallomics* **2017**, *9*, 1483-1500.

(2) (a) Mole, D. R. Iron Homeostasis and Its Interaction with Prolyl Hydroxylases. *Antioxid. Redox Signal*. **2010**, *12*, 445-458. (b) Hirota, K. An intimate crosstalk between iron homeostasis and oxygen metabolism regulated by the hypoxia-inducible factors (HIFs). *Free Radic. Biol. Med*. ***2019***, *133*, 118-129.

(3) (a) Waterman, M. R.; Simpson, E. R. Regulation of the biosynthesis of cytochromes P-450 involved in steroid hormone synthesis. *Mol. Cell. Endocrinol*. **1985**, *39*, 81-89. (b) Rocklin, A. M.; Tierney, D. L.; Kofman, V.; Brunhuber, N. M. W.; Hoffman, B. M.; Christoffersen, R. E.; Reich, N. O.; Lipscomb, J. D.; Que, L., Jr. Role of the nonheme Fe(II) center in the biosynthesis of the plant hormone ethylene. *Proc. Natl. Acad. Sci. U.S.A*. **1999**, *96*, 7905-7909. (c) Silva, B.; Faustino, P. An overview of molecular basis of iron metabolism regulation and the associated pathologies. *Biochim. Biophys. Acta, Mol. Basis Dis*. **2015**, *1852*, 1347-1359.

(4) (a) Zanger, U. M.; Schwab, M. Cytochrome P450 enzymes in drug metabolism: Regulation of gene expression, enzyme activities, and impact of genetic variation. *Pharmacol. Therapeut*. **2013**, *138*, 103-141. (b) Crielaard, B. J.; Lammers, T.; Rivella, S. Targeting iron metabolism in drug discovery and delivery. *Nat. Rev. Drug Discov*. **2017**, *16*, 400-423.

(5) (a) Tang, M.-C.; Zou, Y.; Watanabe, K.; Walsh, C. T.; Tang, Y. Oxidative Cyclization in Natural Product Synthesis. *Chem. Rev*. **2017**, *117*, 5226-5333. (b) Zwick, C. R., III; Renata, H. Harnessing the biocatalytic potential of iron- and α-ketoglutarate-dependent dioxygenases in natural product total synthesis. *Nat. Prod. Rep*. **2020**, *37*, 1065-1079. (c) Ushimaru, R.; Abe, I. Unusual Dioxygen-Dependent Reactions Catalyzed by Nonheme Iron Enzymes in Natural Product Biosynthesis. *ACS. Catal*. **2023**, *13*, 1045-1076. (d) Zhang, X.; Guo, J.; Cheng, F.; Li, S. Cytochrome P450 enzymes in fungal natural product biosynthesis. *Nat. Prod. Rep*. **2021**, *38*, 1072-1099.

(6) (a) Kovaleva, E. G.; Lipscomb, J. D. Versatility of biological non-heme Fe(II) centers in oxygen activation reactions. *Nat. Chem. Biol*. **2008**, *4*, 186-193. (b) Martinez, S.; Hausinger, R. P. Catalytic Mechanisms of Fe(II)- and 2-Oxoglutarate-dependent Oxygenases. *J. Biol. Chem*. **2015**, *290*, 20702-20711. (c) Herr, C. Q.; Hausinger, R. P. Amazing Diversity in Biochemical Roles of Fe(II)/2-Oxoglutarate Oxygenases. *Trends Biochem. Sci*. **2018**, *43*, 517-532. (d) Nakamura, H.; Matsuda, Y.; Abe, I. Unique chemistry of non-heme iron enzymes in fungal biosynthetic pathways. *Nat. Prod. Rep*. **2018**, *35*, 633-645. (e) Timmins, A.; de Visser, S. P. A Comparative Review on the Catalytic Mechanism of Nonheme Iron Hydroxylases and Halogenases. *Catalysts* **2018**, *8*, 314.

(7) (a) Cox, R. J.; Al-Fahad, A. Chemical mechanisms involved during the biosynthesis of tropolones. *Curr. Opin. Chem. Biol*. **2013**, *17*, 532-536. (b) Cox, R. J. Oxidative rearrangements during fungal biosynthesis. *Nat. Prod. Rep*. **2014**, *31*, 1405-1424. (c) Doyon, T. J.; Skinner, K. C.; Yang, D.; Mallik, L.; Wymore, T.; Koutmos, M.; Zimmerman, P. M.; Narayan, A. R. H. Radical Tropolone Biosynthesis. *ChemRxiv* Preprint, 2020, https://chemrxiv.org/articles/preprint/Radical_Tropolone_Biosynthesis/12780044/1.

(8) Yang, D.; Chiang, C.-H.; Wititsuwannakul, T.; Brooks, C. L., III; Zimmerman, P. M.; Narayan, A. R. H. Engineering the Reaction Pathway of a Non-heme Iron Oxygenases Using Ancestral Sequence Reconstruction. *J. Am. Chem. Soc*. **2024**, *submitted*.

(9) Guo, H.; Roman, D.; Beemelmanns, C. Tropolone natural products. *Nat. Prod. Rep*. **2019**, *36*, 1137-1155.

(10) (a) Stevens, H. C.; Reich, D. A.; Brandt, D. R.; Fountain, K. R.; Gaughan, E. J. A New Tropolone Synthesis via Dichloroketene. *J. Am. Chem. Soc*. **1965**, *87*, 5257-5359. (b) Barbier, M.; Barton, D. H. R.; Devys, M.; Topgi, R. S. A simple synthesis of the tropone nucleus. *J. Chem. Soc., Chem. Commun*. **1984**, 743-744. (c) Barbier, M.; Barton, D. H. R.; Devys, M.; Topgi, R. S. A simple synthesis of tropoones and related compounds. *Tetrahedron* **1987**, *43*, 5031-5038. (d) Reisman, S. E.; Nani, R. R.; Levin, S. Buchner and Beyond: Arene Cyclopropanation as Applied to Natural Product Total Syntesis. *Synlett* **2011**, 2437-2442. (e) Meck, C.; D'Erasmo, M. P.; Hirsch, D. R.; Murelli, R. P. The biology and synthesis of α-hydroxytropolones. *Med. Chem. Commun*. **2014**, *5*, 842-852. (f) Liu, N.; Song, W.; Schienebeck, C. M.; Zhang, M.; Tang, W. Synthesis of naturally occurring tropones and tropolones. *Tetrahedron* **2014**, *70*, 9281-9305. (g) Hirsch, D. R.; Schiavone, D. V.; Berkowitz, A. J.; Morrison, L. A.; Masaoka, T.; Wilson, J. A.; Lomonosova, E.; Zhao, H.; Patel, B. S.; Dalta, S. H.; Hoft, S. G.; Majidi, S. J.; Pal, R. K.; Gallicchio, E.; Tang, L.; Tavis, J. E.; Le Grice, S. F. J.; Beutler, J. A.; Murelli, R. P. Synthesis and biological assessment of 3,7-dihydroxytropolones. *Org. Biomol. Chem*. **2018**, *16*, 62-69.

(11) Walsh, C. T.; Moore, B. S. Enzymatic Cascade Reactions in Biosynthesis. *Angew. Chem., Int. Ed*. **2019**, *58*, 6846-6879.

(12) Gerlt, J. A.; Babbitt, P. C. Divergent Evolution of Enzymatic Function: Mechanistically Diverse Superfamilies and Functionally Distinct Superfamilies. *Annu. Rev. Biochem*. **2001**, *70*, 209-246.

(13) (a) Borowski, T.; Bassan, A.; Siegbahn, P. E. M. Mechanism of Dioxygen Activation in 2-Oxoglutarate-Dependent Enzymes: A Hybrid DFT Study. *Chem. Eur. J*. **2004**, *10*, 1031-1041. (b) Wójcik, A.; Radoń, M.; Borowski, T. Mechanism of O_2 Activation by α-Ketoglutarate Depen-

dent Oxygenases Revisited. A Quantum Chemical Study. *J. Phys. Chem. A* **2016**, *120*, 1261-1274. (c) Kal, S.; Que, L., Jr. Dioxygen activation by nonheme iron enzymes with the 2-His-1-carboxylate facial triad that generate high-valent oxoiron oxidants. *J. Biol. Inorg. Chem*. **2017**, *22*, 339-365. (d) Solomon, E. I.; DeWeese, D. E.; Babicz, J. T., Jr. Mechanisms of O_2 Activation by Mononuclear Non-Heme Iron Enzymes. *Biochemistry* **2021**, *60,* 3497-3506.

(14) (a) Krebs, C.; Fujimori, D. G.; Walsh, C. T.; Bollinger, J. M., Jr. Non-Heme Fe(IV)–Oxo Intermediates. *Acc. Chem. Res*. **2007**, *40*, 484-492. (b) Solomon, E. I.; Light, K. M.; Liu, L. V.; Srnec, M.; Wong, S. D. Geometric and Electronic Structure Contributions to Function in Non-heme Iron Enzymes. *Acc. Chem. Res*. **2013**, *46*, 2725-2739.

(15) (a) Valegård, K.; van Scheltinga, A. C. T.; Dubus, A.; Ranghino, G.; Öster, L. M.; Hajdu, J.; Andersson, I. *Nat. Struct. Mol. Biol*. **2004**, *11*, 95-101. (b) Yan, L.; Liu, Y. Insights into the Mechanism and Enantioselectivity in the Biosynthesis of Ergot Alkaloid Cycloclavine Catalyzed by Aj_EasH from *Aspergillus japonicus*. *Inorg. Chem*. **2019**, *58*, 13771-13781. (c) Li, H.; Liu, Y. Mechanistic Investigation of Isonitrile Formation Catalyzed by the Nonheme Iron/α-KG-Dependent Decarboxylase (ScoE). *ACS Catal*. **2020**, *10*, 2942-2957.

(16) (a) de Visser, S. P. Second-Coordination Sphere Effects on Selectivity and Specificity of Heme and Nonheme Iron Enzymes. *Chem. Eur. J*. **2020**, *26*, 5308-5327. (b) de Visser, S. P.; Lin, Y.-T.; Ali, H. S.; Bagha, U. K.; Mukherjee, G.; Sastri, C. V. Negative catalysis / non-Bell-Evans-Polanyi reactivity by metalloenzymes: Examples from mononuclear heme and non-heme iron oxygenases. *Coord. Chem. Rev*. **2021**, *439*, 213914. (c) Wojdyla, Z.; Borowski, T. Properties of the Reactants and Their Interactions within and with the Enzyme Binding Cavity Determine Reaction Selectivities. The Case of Fe(II)/2-Oxoglutarate Dependent Enzymes. *Chem. Eur. J.* **2022**, *28*, e202104106.

(17) (a) Dunham, N. P.; Chang, W.-c.; Mitchell, A. J.; Martinie, R. J.; Zhang, B.; Bergman, J. A.; Rajakovich, L. J.; Wang, B.; Silakov, A.; Krebs, C.; Boal, A. K.; Bollinger, J. M., Jr. Two Distinct Mechanisms for C–C Desaturation by Iron(II)- and 2-(Oxo)glutarate-Dependent Oxygenases: Importance of α-Heteroatom Assistance. *J. Am. Chem. Soc*. **2018**, *140*, 7116-7126. (b) Dun-

ham, N. P.; Mitchell, A. J.; Del Río Pantoja, J. M.; Krebs, C.; Bollinger, J. M., Jr.; Boal, A. K. α-Amine Desaturation of D-Arginine by the Iron(II)- and 2-(Oxo)glutarate-Dependent L-Arginine 3-Hydroxylase, VioC. *Biochemistry* **2018**, *57*, 6479-6488. (c) Tang, H.; Wu, M. H.; Lin, H. Y.; Han, M. R.; Tu, Y. H.; Yang, Z. J.; Chien, T. C.; Chan, N. L.; Chang, W.-c. Mechanistic analysis of carbon–carbon bond formation by deoxypodophyllotoxin synthase. *Proc. Natl. Acad. Sci. U.S.A*. **2022**, *119*, e2113770119. (d) Tao, H.; Ushimaru, R.; Awakawa, T.; Mori, T.; Uchiyama, M.; Abe, I. Stereoselectivity and Substrate Specificity of the Fe(II)/α-ketoglutarate-Dependent Oxygenase TqaL. *J. Am. Chem. Soc*. **2022**, *144*, 21512-21520. (e) Chen, T.-Y.; Zheng, Z.; Zhang, X.; Chen, J.; Cha, L.; Tang, Y.; Guo, Y.; Zhou, J.; Wang, B.; Liu, H.-w.; Chang, W.-c. Deciphering the Reaction Pathway of Mononuclear Iron Enzyme-Catalyzed N≡C Triple Bond Formation in Isocyanide Lipopeptide and Polyketide Biosynthesis. *ACS Catal*. **2022**, *12*, 2270-2279. (f) Ali, H. S.; Warwicker, J.; de Visser, S. P. How Does the Nonheme Iron Enzyme NapI React through L-Arginine Desaturation Rather Than Hydroxylation? A Quantum Mechanics/Molecular Mechanics Study. *ACS Catal*. **2023**, *13*, 10705-10721. (g) Cha, L.; Paris, J. C.; Zanella, B.; Spletzer, M.; Yao, A.; Guo, Y.; Chang, W.-c. Mechanistic Studies of Aziridine Formation Catalyzed by Mononuclear Non-Heme Iron Enzymes. *J. Am. Chem. Soc*. **2023**, *145*, 6240-6246.

(18) Field, M. J.; Bash, P. A.; Karplus, M. A combined quantum mechanical and molecular mechanical potential for molecular dynamics simulations. *J. Comput. Chem*. **1990**, *11*, 700-733.

(19) (a) Senn, H. M.; Thiel, W. QM/MM Methods for Biomolecular Systems. *Angew. Chem., Int. Ed*. **2009**, *48*, 1198-1229. (b) van der Kamp, M. W.; Mullholland, A. J. Combined Quantum Mechanics/Molecular Mechanics (QM/MM) Methods in Computational Enzymology. *Biochemistry* **2013**, *52*, 2708-2728. (c) Quesne, M. G.; Borowski, T.; de Visser, S. P. Quantum Mechanics/Molecular Mechanics Modeling of Enzymatic Processes: Caveats and Breakthroughs. *Chem. Eur. J*. **2016**, *22*, 2562-2581.

(20) (a) Waheed, S. O.; Chaturvedi, S. S.; Karabencheva-Christova, T. G.; Christov, C. Z. Catalytic Mechanism of Human Ten-Eleven Translocation-2 (TET2) Enzyme: Effects of Conformational Changes, Electric Field, and Mutations. *ACS Catal.* **2021**, *11*, 3877-3890. (b) Waheed, S.

O.; Varghese, A.; Chaturvedi, S. S.; Karabencheva-Christova, T. G.; Christov, C. Z. How Human TET2 Enzyme Catalyzes the Oxidation of Unnatural Cytosine Modifications in Double-Stranded DNA. *ACS Catal.* **2022**, *12*, 5327-5344. (c) Chaturvedi, S. S.; Jaber Sathik Rifayee, S. B.; Waheed, S. O.; Wildey, J.; Warner, C.; Schofield, C. J.; Karabencheva-Christova, T. G.; Christov, C. Z. Can Second Coordination Sphere and Long-Range Interactions Modulate Hydrogen Atom Transfer in a Non-Heme Fe(II)-Dependent Histone Demethylase?. *JACS Au* **2022**, *2*, 2169-2186. (d) Jaber Sathik Rifayee, S. B.; Chaturvedi, S. S.; Warner, C.; Wildey, J.; White, W.; Thompson, M.; Schofield, C. J.; Christov, C. Z. Catalysis by KDM6 Histone Demethylases – A Synergy between the Non-Heme Iron(II) Center, Second Coordination Sphere, and Long-Range Interactions. *Chem. Eur. J.* **2023**, *29*, e202301305.

(21) Humphrey, W.; Dalke, A; Schulten, K., VMD - Visual Molecular Dynamics. *J. Molec. Graphics* **1996**, *14*, 33-38.

(22) https://iqmol.org (accessed July 29, 2024).

(23) Jumper, J.; Evans, R.; Pritzel, A.; Green, T.; Figurnov, M.; Ronneberger, O.; Tunyasuvunakool, K.; Bates, R.; Žídek, A.; Potapenko, A.; Bridgland, A.; Meyer, C.; Kohl, S. A. A.; Ballard, A. J.; Cowie, A.; Romera-Paredes, B.; Nikolov, S.; Jain, R.; Adler, J.; Back, T.; Petersen, S.; Reiman, D.; Clancy, E.; Zielinski, M.; Steinegger, M.; Pacholska, M.; Berghammer, T.; Bodenstein, S.; Silver, D.; Vinyals, O.; Senior, A. W.; Kavukcuoglu, K.; Kohli, P.; Hassabis, D. Highly accurate protein structure prediction with AlphaFold. *Nature* **2021**, 596, 583-589.

(24) Berman, H. M.; Westbrook, J.; Feng, Z.; Gilliland, G.; Bhat, T. N.; Weissig, H.; Shindyalov, I. N.; Bourne, P. E. The Protein Data Bank. *Nucl. Acids Res*. **2000**, *28*, 235-242.

(25) Li, W.; Zhang, T.; Ding, J. Molecular basis for the substrate specificity and catalytic mechanism of thymine-7-hydroxylase in fungi. *Nucleic Acids Res*. **2015**, *43*, 10026-10038.

(26) (a) Trott, O.; Olson, A. J. AutoDock Vina: Improving the speed and accuracy of docking with a new scoring function, efficient optimization, and multithreading. *J. Comput. Chem*. **2009**, *31*, 455-461. (b) Eberhardt, J.; Santos-Martins, D.; Tillack, A. F.; Forli, S. AutoDock Vina

1.2.0: New Docking Methods, Expanded Force Field, and Python Bindings. *J. Chem. Inf. Model*. **2021**, *61*, 3891-3898.

(27) Jo, S.; Kim, T.; Iyer, V. G.; Lm, W. CHARMM-GUI: A web-based graphical user interface for CHARMM. *J. Comput. Chem*. **2008**, *29*, 1859-1865.

(28) (a) Olsson, M. H. M.; Søndergaard, C. R.; Rostkowski, M.; Jensen, J. H. PROPKA3: Consistent Treatment of Internal and Surface Residues in Empirical pK_a Predictions. *J. Chem. Theory. Comput*. **2011**, *7*, 525-537. (b) Søndergaard, C. R.; Olsson, M. H. M.; Rostkowski, M.; Jensen, J. H. Improved Treatment of Ligands and Coupling Effects in Empirical Calculation and Rationalization of pK_a Values. *J. Chem. Theory Comput*. **2011**, *7*, 2284-2295.

(29) Darden, T.; York, D.; Pedersen, L. Particle mesh Ewald: An $N\cdot\log(N)$ method for Ewald sums in large systems. *J. Chem. Phys*. **1993**, *98*, 10089-10092.

(30) (a) Vanommeslaeghe, K.; Hatcher, E.; Acharya, C.; Kundu, S.; Zhong, S.; Shim, J.; Darian, E.; Guvench, O.; Lopes, P.; Vorobyov, I.; Mackerell, A. D., Jr. CHARMM general force field: A force field for drug-like molecules compatible with the CHARMM all-atom additive biological force field. *J. Comput. Chem*. **2010**, *31*, 671-690. (b) Yu, W.; He, X.; Vanommeslaeghe, K.; Mackerell, A. D., Jr. Extension of the CHARMM general force field to sulfonyl-containing compounds and its utility in biomolecular simulations. *J. Comput. Chem*. **2012**, *33*, 2451-2468.

(31) Pang, X.; Han, K.; Cui, Q. A simple but effective modeling strategy for structural properties of non-heme Fe(II) sites in proteins: Test of force field models and application to proteins in the AlkB family. *J. Comput. Chem*. **2013**, *34*, 1620-1635.

(32) Huang, J.; Mackerell, A. D., Jr. CHARMM36 all-atom additive protein force field: Validation based on comparison to NMR data. *J. Comput. Chem*. **2013**, *34*, 2135-2145.

(33) Eastman, P.; Swails, J.; Chodera, J. D.; Mcgibbon, R. T.; Zhao, Y.; Beauchamp, K. A.; Wang, L.-P.; Simmonett, A. C.; Harrigan, M. P.; Stern, C. D.; Wiewiora, R. P.; Brooks, B. R.; Pande, V. S. OpenMM 7: Rapid development of high performance algorithms for molecular dynamics. *Plos Comput. Biol*. **2017**, *13*, e1005659.

(34) Loncharich, R. J.; Brooks, B. R.; Pastor, R. W. Langevin dynamics of peptides: The frictional dependence of isomerization rates of *N*-acetylalanyl-*N*′-methylamide. *Biopolymers* **1992**, *32*, 523-535.

(35) Bondi, A. van der Waals Volumes and Radii. *J. Phys. Chem*. **1964**, *68*, 441-451.

(36) (a) Jeffrey, G. A. *An Introduction to Hydrogen Bonding*; Oxford University Press: New York, 1997; Chapter 2. (b) Arunan, E.; Desiraju, G. R.; Klein, R. A.; Sadlej, J.; Scheiner, S.; Alkorta, I.; Clary, D. C.; Crabtree, R. H.; Dannenber, J. J.; Hobza, P.; Kjaergaard, H. G.; Legon, A. C.; Mennuci, B.; Nesbitt, D. J. Definition of the hydrogen bond: An account (IUPAC Technical Report). *Pure Appl. Chem*. **2011**, *83*, 1619-1636. (c) Arunan, E.; Desiraju, G. R.; Klein, R. A.; Sadlej, J.; Scheiner, S.; Alkorta, I.; Clary, D. C.; Crabtree, R. H.; Dannenber, J. J.; Hobza, P.; Kjaergaard, H. G.; Legon, A. C.; Mennuci, B.; Nesbitt, D. J. Definition of the hydrogen bond (IUPAC Recommendations 2011). *Pure Appl. Chem*. **2011**, *83*, 1637-1641.

(37) (a) Field, M. J. *A Practical Introduction to the Simulation of Molecular Systems*, 2nd ed.; Cambridge University Press: Cambridge, United Kingdom, 2007. (b) Field, M. J. The pDynamo Program for Molecular Simulations using Hybrid Quantum Chemical and Molecular Potentials. *J. Chem. Theory Comput*. **2008**, *4*, 1151-1161.

(38) (a) Nocedal, J. Updating Quasi-Newton Matrices with Limited Storage. *Math. Comput*. **1980**, *35*, 773-782. (b) Liu, D. C.; Nocedal, J. On the Limited Memory BFGS method for Large Scale Optimization. *Math. Program*. **1989**, *45*, 503-528.

(39) Shao, Y.; Gan, Z.; Epifanovsky, E.; Gilbert, A. T. B.; Wormit, M.; Kussmann, J.; Lange, A. W.; Behn, A.; Deng, J.; Feng, X.; Ghosh, D.; Goldey, M.; Horn, P. R.; Jacobson, L. D.; Kaliman, I.; Khaliullin, R. Z.; Kuś, T.; Landau, A.; Liu, J.; Proynov, E. I.; Rhee, Y. M.; Richard, R. M.; Rohrdanz, M. A.; Steele, R. P.; Sundstrom, E. J.; Woodcock, H. L.; Zimmerman, P. M.; Zuev, D.; Albrecht, B.; Alguire, E.; Austin, B.; Beran, G. J. O.; Bernard, Y. A.; Berquist, E.; Brandhorst, K.; Bravaya, K. B.; Brown, S. T.; Casanova, D.; Chang, C.-M.; Chen, Y.; Chien, S. H.; Closser, K. D.; Crittenden, D. L.; Diedenhofen, M.; DiStasio, R. A.; Do, H.; Dutoi, A. D.; Edgar, R. G.; Fatehi, S.; Fusti-Molnar, L.; Ghysels, A.; Golubeva-Zadorozhnaya, A.; Gomes, J.;

Hanson-Heine, M. W. D.; Harbach, P. H. P.; Hauser, A. W.; Hohenstein, E. G.; Holden, Z. C.; Jagau, T.-C.; Ji, H.; Kaduk, B.; Khistyaev, K.; Kim, J.; Kim, J.; King, R. A.; Klunzinger, P.; Kosenkov, D.; Kowalczyk, T.; Krauter, C. M.; Lao, K. U.; Laurent, A. D.; Lawler, K. V.; Levchenko, S. V.; Lin, C. Y.; Liu, F.; Livshits, E.; Lochan, R. C.; Luenser, A.; Manohar, P.; Manzer, S. F.; Mao, S.-P.; Mardirossian, N.; Marenich, A. V.; Maurer, S. A.; Mayhall, N. J.; Neuscamman, E.; Oana, C. M.; Olivares-Amaya, R.; O'Neill, D. P.; Parkhill, J. A.; Perrine, T. M.; Peverati, R.; Prociuk, A.; Rehn, D. R.; Rosta, E.; Russ, N. J.; Sharada, S. M.; Sharma, S.; Small, D. W.; Sodt, A.; Stein, T.; Stück, D.; Su, Y.-C.; Thom, A. J. W.; Tsuchimochi, T.; Vanovschi, V.; Vogt, L.; Vydrov, O.; Wang, T.; Watson, M. A.; Wenzel, J.; White, A.; Williams, C. F.; Yang, J.; Yeganeh, S.; Yost, S. R.; You, Z.-Q.; Zhang, I. Y.; Zhang, X.; Zhao, Y.; Brooks, B. R.; Chan, G. K. L.; Chipman, D. M.; Cramer, C. J.; Goddard, W. A.; Gordon, M. S.; Hehre, W. J.; Klamt, A.; Schaefer, H. F.; Schmidt, M. W.; Sherrill, C. D.; Truhlar, D. G.; Warshel, A.; Xu, X.; Aspuru Guzik, A.; Baer, R.; Bell, A. T.; Besley, N. A.; Chai, J.-D.; Dreuw, A.; Dunietz, B. D.; Furlani, T. R.; Gwaltney, S. R.; Hsu, C.-P.; Jung, Y.; Kong, J.; Lambrecht, D. S.; Liang, W.; Ochsenfeld, C.; Rassolov, V. A.; Slipchenko, L. V.; Subotnik, J. E.; Van Voorhis, T.; Herbert, J. M.; Krylov, A. I.; Gill, P. M. W.; Head-Gordon, M. Advances in molecular quantum chemistry contained in the Q-Chem 4 program package. *Mol. Phys*. **2015**, *113*, 184-215.

(40) (a) Lee, C.; Yang, W.; Parr, R. G. Development of the Colle-Salvetti correlation-energy formula into a functional of the electron density. *Phys. Rev. B: Condens. Matter Mater. Phys*. **1988**, *37*, 785-789. (b) Becke, A. D. Density-functional thermochemistry. III. The role of exact exchange. *J. Chem. Phys*. **1993**, *98*, 5648-5652. (c) Stephens, P. J.; Devlin, F. J.; Chabalowski, C. F.; Frisch, M. J. *Ab Initio* Calculation of Vibrational Absorption and Circular Dichroism Spectra Using Density Functional Force Fields. *J. Phys. Chem*. **1994**, *98*, 11623-11627.

(41) Grimme, S.; Ehrlich, S.; Goerigk, L. Effect of the damping function in dispersion corrected density functional theory. *J. Comput. Chem*. **2011**, *32*, 1456-1465.

(42) (a) Hariharan, P. C.; Pople, J. A. The Influence of Polarization Functions on Molecular Orbital Hydrogenation Energies. *Theor. Chim. Acta* **1973**, *28*, 213-222. (b) Petersson, G. A.; Ben-

nett, A.; Tensfeldt, T. G.; Al-Laham, M. A.; Shirley, W. A.; Mantzaris, J. A complete basis set model chemistry. I. The total energies of closed-shell atoms and hydrides of the first-row elements. *J. Chem. Phys*. **1988**, *89*, 2193-2218. (c) Petersson, G. A.; Al-Laham, M. A. A complete basis set model chemistry. II. Open-shell systems and the total energies of the first-row atoms. *J. Chem. Phys*. **1991**, *94*, 6081-6090.

(43) MacKerell, A. D., Jr.; Babavali, N.; Foloppe, N. Development and Current Status of the CHARMM Force Field for Nucleic Acids. *Biopolymers* **2000**, *56*, 257-265.

(44) (a) Bakowies, D.; Thiel, W. Hybrid Models for Combined Quantum Mechanical and Molecular Mechanical Approaches. *J. Phys. Chem*. **1996**, *100*, 10580-10594. (b) Groenhof, G. Introduction to QM/MM simulations. *Methods. Mol. Bol*. **2013**, *924*, 43-66.

(45) (a) Godfrey, E.; Porro, C. S.; de Visser, S. P. Comparative Quantum Mechanics/Molecular Mechanics (QM/MM) and Density Functional Theory Calculations on the Oxo–Iron Species of Taurine/α-Ketoglutarate Dioxygenase. *J. Phys. Chem. A* **2008**, *112*, 2464-2468. (b) Huang, J.; Li, C.; Wang, B.; Sharon, D. A.; Wu, W.; Shaik, S. Selective Chlorination of Substrates by the Halogenase SyrB2 Is Controlled by the Protein According to a Combined Quantum Mechanics/ Molecular Mechanics and Molecular Dynamics Study. *ACS Catal*. **2016**, *6*, 2694-2704. (c) Ghafoor, S.; Mansha, A.; de Visser, S. P. Selective Hydrogen Atom Abstraction from Dihydroflavonol by a Nonheme Iron Center Is the Key Step in the Enzymatic Flavonol Synthesis and Avoids Byproducts. *J. Am. Chem. Soc.* **2019**, *141*, 20278-20292. (d) Phung, Q. M.; Martín-Fernández, C.; Harvey, J. N.; Feldt, M. Ab Initio Calculations for Spin-Gaps of Non-Heme Iron Complexes. *J. Chem. Theory. Comput*. **2019**, *15*, 4297-4304. (e) Geng, C. L.; Ye, S.; Neese, F. Analysis of Reaction Channels for Alkane Hydroxylation by Nonheme Iron(IV)–Oxo Complexes. *Angew. Chem., Int. Ed*. **2010**, *49*, 5717-5720. (f) Borowski, T.; Noack, H.; Radoń, M.; Zych, K.; Siegbahn, P. E. M. Mechanism of Selective Halogenation by SyrB2: A Computational Study. *J. Am. Chem. Soc*. **2010**, *132*, 12887-12898. (g) Mehmood, R.; Qi, H. W.; Steeves, A. H.; Kulik, H. J. The Protein's Role in Substrate Positioning and Reactivity for Biosynthetic Enzyme Complexes: The Case of SyrB2/SyB1. *ACS Catal*. **2019**, *9*, 4930-4943. (h) Mehmood, R.; Vennelakanti, V.; Kulik, H. J. Spectrosco-

pically Guided Simulations Reveal Distinct Strategies for Positioning Substrates to Achieve Selectivity in Nonheme Fe(II)/α-Ketoglutarate-Dependent Halogenases. *ACS Catal*. **2021**, *11*, 12394-12408. (i) Kastner, D.; Nandy, A.; Mehmood, R.; Kulik, H. J. Mechanistic Insights into Substrate Positioning That Distinguish Non-heme Fe(II)/α-Ketoglutarate-Dependent Halogenases and Hydroxylases. *ACS Catal*. **2023**, *13*, 2489-2501.

(46) (a) Riggs-Gelasco, P. J.; Price, J. C.; Guyer, R. B.; Brehm, J. H.; Barr, E. W.; Bollinger, J. M., Jr.; Krebs, C. EXAFS Spectroscopic Evidence for an Fe=O Unit in the Fe(IV) Intermediate Observed during Oxygen Activation by Taurine:α-Ketoglutarate Dioxygenase. *J. Am. Chem. Soc.* **2004**, *126*, 8108-8109. (b) Bollinger, J. M., Jr.; Price, J. C.; Hoffart, L. M.; Barr, E. W.; Krebs, C. Mechanism of Taurine: α-Ketoglutarate Dioxygenase (TauD) from *Escherichia coli*. *Eur. J. Inorg. Chem.* **2005**, 4245-4254. (c) Hoffart, L. M.; Barr, E. W.; Guyer, R. B.; Bollinger, J. M., Jr.; Krebs, C. Direct spectroscopic detection of a C–H-cleaving high-spin Fe(IV) complex in a prolyl-4-hydroxylase. *Proc. Natl. Acad. Sci. U.S.A.* **2006**, *103*, 14738-14743.

(47) (a) Schlitter, J.; Swegat, W.; Mülders, T. Distance-type reaction coordinates for modelling activated processes. *J. Mol. Model* **2001**, *7*, 171-177. (b) Schlitter, J. Constraint methods for determining pathways and free energy of activated processes. *Eur. Phys. J. Special Topics* **2011**, *200*, 91-105.

(48) Contreras-García, J.; Johnson, E. R.; Keinan, S.; Chaudret, R.; Piquemal, J.-P.; Beratan, D. N.; Yang, W. NCIPLOT: A Program for Plotting Noncovalent Interaction Regions. *J. Chem. Theory Comput*. **2011**, *7*, 625-632.

(49) (a) Dederichs, P. H.; Blügel, S.; Zeller, R.; Akai, H. Ground States of Constrained Systems: Application to Cerium Impurities. *Phys. Rev. Lett*. **1984**, *53*, 2512-2515. (b) Wu, Q.; Van Voorhis, T. Direct optimization method to study constrained systems within density-functional theory. *Phys. Rev. A* **2005**, *72*, 024502. (c) Kaduk, B.; Kowalczyk, T.; Van Voorhis, T. Constrained Density Functional Theory. *Chem. Rev*. **2012**, *112*, 321-370.

(50) Skinner, K. C.; Kammeraad, J. A.; Wymore, T.; Narayan, A. R. H.; Zimmerman, P. M. Simulating Electron Transfer Reactions in Solution: Radical-Polar Crossover. *J. Phys. Chem. B* **2023**, *127*, 10097-10107.

(51) (a) Que, L., Jr. One motif ─ many different reactions. *Nat. Struct. Biol.* **2000**, *7*, 182-184. (b) Koehntop, K. D.; Emerson, J. P.; Que, L., Jr. The 2-His-1-carboxylate facial triad: a versatile platform for dioxygen activation by mononuclear non-heme iron(II) enzymes. *JBIC, J. Biol. Inorg. Chem.* **2005**, *10*, 87-93.

(52) (a) Hirao, H.; Kumar, D.; Que, L., Jr.; Shaik, S. Two-State Reactivity in Alkane Hydroxylation by Non-Heme Iron–Oxo Complexes. *J. Am. Chem. Soc.* **2006**, *128*, 8590-8606. (b) Ye, S.; Neese, F. Nonheme oxo–iron(IV) intermediates form an oxyl radical upon approaching the C–H bond activation transition state. *Proc. Natl. Acad. Sci. U.S.A.* **2011**, *108*, 1228-1233 (c) Ye, S.; Geng, C.-Y.; Shaik, S.; Neese, F. Electronic structure analysis of multistate reactivity in transition metal catalyzed reactions: the case of C–H bond activation by non-heme iron(IV)–oxo cores. *Phys. Chem. Chem. Phys.* **2013**, *15*, 8017-8030.

(53) (a) Beckwith, A. L. J.; O'Shea, D. M.; Westwood, S. W. Rearrangement of Suitably Constituted Aryl, Alkyl, or Vinyl Radicals by Acyl or Cyano Group Migration. *J. Am. Chem. Soc*. **1988**, *110*, 2565-2575. (b) Dowd, P.; Choi, S.-C. Novel free radical ring-expansion reactions. *Tetrahedron* **1989**, *45*, 77-90. (c) Dowd, P.; Zhang, W. Free Radical-Mediated Ring Expansion and Related Annulations. *Chem. Rev*. **1993**, *93*, 2091-2115. (d) Dowd, P.; Choi, S.-C. Free radical ring-expansion leading to novel six- and seven-membered heterocycles. *Tetrahedron Lett*. **1989**, *30*, 6129-6132.

(54) Singha, T.; Rouf Samim Mondal, A.; Midya, S.; Prasad Hari, D. The Dowd-Beckwith Reaction: History, Strategies, and Synthetic Potential. *Chem. Eur. J*. **2022**, *28*, e202202025.

(55) Huang, X.; Groves, J. T. Beyond ferry-mediated hydroxylation: 40 years of the rebound mechanism and C–H activation. *JBIC, J. Biol. Inorg. Chem.* **2017**, *22*, 185-207.

(56) Zaragoza, J. P. T.; Cummins, D. C.; Mubarak, M. Q. E.; Siegler, M. A.; de Visser, S. P.; Goldberg, D. P. Hydrogen Atom Abstraction by High-Valent Fe(OH) Versus Mn(OH) Porphy-

rinoid Complexes: Mechanistic Insights from Experimental and Computational Studies. *Inorg. Chem.* **2019**, *58*, 16761-16770.

(57) Borowski, T.; Wójcik, A.; Miłaczewska, A.; Georgiev, V.; Blomberg, M. R. A.; Siegbahn, P. E. M. The alkenyl migration mechanism catalyzed by extradiol dioxygenases: a hybrid DFT study. *JBIC, J. Biol. Inorg. Chem.* **2012**, *17*, 881-990.

(58) (a) Ess, D. H.; Houk, K. N. Distortion/Interaction Energy Control of 1,3-Dipolar Cycloaddition Reactivity. *J. Am. Chem. Soc.* **2007**, *129*, 10646-10647. (b) Bickelhaupt, F. M.; Houk, K. N. Analyzing Reaction Rates with the Distortion/Interaction-Activation Strain Model. *Angew. Chem., Int. Ed.* **2017**, *56*, 10070-10086.

(59) (a) Song, Z.-L.; Fan, C.-A.; Tu, Y.-Q. Semipinacol Rearrangement in Natural Product Systhesis. *Chem. Rev*. **2011**, *111*, 7523-7556. (b) Zhang, X.-M.; Li, B.-S.; Wang, S.-H.; Zhang, K.; Zhang, F.-M.; Tu, Y.-Q. Recent development and applications of semipinacol rearrangement reactions. *Chem. Sci*. **2021**, *12*, 9262-9274.

(60) The Fe–N_5(His270) distances of **4** + [Fe(III)–OH] of variants 1, 2, and 3 are respectively similar (2.02 Å vs. 2.08 Å vs. 2.03 Å; Table 3), controlled by hydrogen bonding motifs summarized in Section S4 (SI). However, the ligand binding energies of His270 nicely trend the energy gaps (ΔE_a) between radical ring-expansion and rebound hydroxylation (Figure 10 and Table 4).

(61) (a) Appleton, T. G.; Clark, H. C.; Manzer, L. E. The *trans*-influence: its measurement and significance. *Coord. Chem. Rev*. **1973**, *10*, 335-422. (b) Coe, B. J.; Glenwright, S. J. Trans-effects in octahedral transition metal complexes. *Coord. Chem. Rev*. **2000**, *203*, 5-80.

(62) Although the ligand binding energy of the hydroxyl ligand of **4** + [Fe(III)–OH] of variant 3 is higher than those of variants 1 and 2 (152.9 kcal/mol vs. 134.4-135.8 kcal/mol; Table 4), their Fe–O_1(OH) distances are respectively similar (1.78 Å vs. 1.79 and 1.79 Å; Table 3). This emphasizes that the Fe–O_1(OH) bonds can be perturbed by the hydrogen bond between Arg191 and the Fe(III)–OH center, in particular for the strong Arg191–OH hydrogen bond in variant 3.

Table of Contents Graphic